nature portfolio
https://doi.org/10.1038/s41586-023-06849-0

# Supplementary information

# $SO_2$, silicate clouds, but no $CH_4$ detected in a warm Neptune

In the format provided by the authors and unedited

# Supplementary information

## 1. JWST MIRI observations and data processing

WASP-107b was observed with the Low-Resolution Spectrometer (LRS [35]) of the Mid-Infrared Instrument (MIRI [36]) on board the JWST on the 19 – 20 January 2023. The data is part of the GTO program under program identifier (PID) 1280 (P.I. P.O. Lagage). The observation started on 19 January at 18:25 UT, in a time-series of 4546 integrations lasting 8h14m, starting approximately 4h50m before the centre of the WASP-107b transit. This total time duration includes the out-of-transit time, ∼30 min of detector settling time, and additional time to accommodate scheduling flexibility.

The data was acquired using the `SLITLESSPRISM` subarray and the `FASTR1` readout mode [35,37]. The integrations consisted of 40 groups (or frames as the MIRI instrument uses 1 frame per group). With this particular number of frames, a maximum signal level of about 75% of the saturation level is reached, ensuring that a photon-noise limited signal is measured while still avoiding the strongest non-linearity effects occurring for signals approaching saturation.

The data processing began with the uncalibrated raw data products retrieved from the Barbara A. Mikulski Archive for Space Telescopes (MAST; `https://archive.stsci.edu/`). In order to ensure results that are not influenced by the calibration or potential uncorrected instrumental systematics, we performed three independent data reductions and light curve analyses. In short, our reductions are based on the `CASCADe` reduction package [11], that was used both for the JWST MIRI and the HST/WFC3 data (Sect. 1.1), the `Eureka!` package [12] (Sect. 1.2) and the `TEATRO` package (see Sect. 1.3). To ensure a correct relative flux calibration, we derived and applied a specific non-linearity correction of the ramps (see Sect. 1.4). The outcomes of the three data reduction methods are compared in Sect. 1.5.

Each method extracted 51 spectroscopic light curves between 4.61 and 11.83 $\mu$m with a 0.15 $\mu$m bin width. Suppl. Inf. Figure 1 shows the `CASCADe` MIRI/LRS transit observation of WASP-107b. The shorter wavelength channels (<7 $\mu$m) show the strongest (downward) drift at the start of the spectral time series, consistent with the behaviour observed in the MIRI/LRS data of the transit of L168-9b [11]. At the longest wavelengths (>11 $\mu$m), a slight upward drift can be observed, although at a much lower amplitude compared to the short wavelength channels. Note that longward of 10 $\mu$m, the noise substantially increases due to a decreasing response of the instrument.

The `SLITLESSPRSIM` subarray covers parts of 3 distinctive regions on the MIRI imager detector. For wavelengths shorter than 10.5 $\mu$m the spectra fall within the Lyot coronographic subarray. For wavelengths between 10.5 $\mu$m and about 11 $\mu$m the LRS spectra fall on an area of the detector covered by the focal plane mask, and at longer wavelengths in the subarray of one of the 4 quadrant phase mask coronographs. Prior operations of the MIRI imager detector (i.e. Exposures with different duration and filter wheel position or idling operation), may impact the

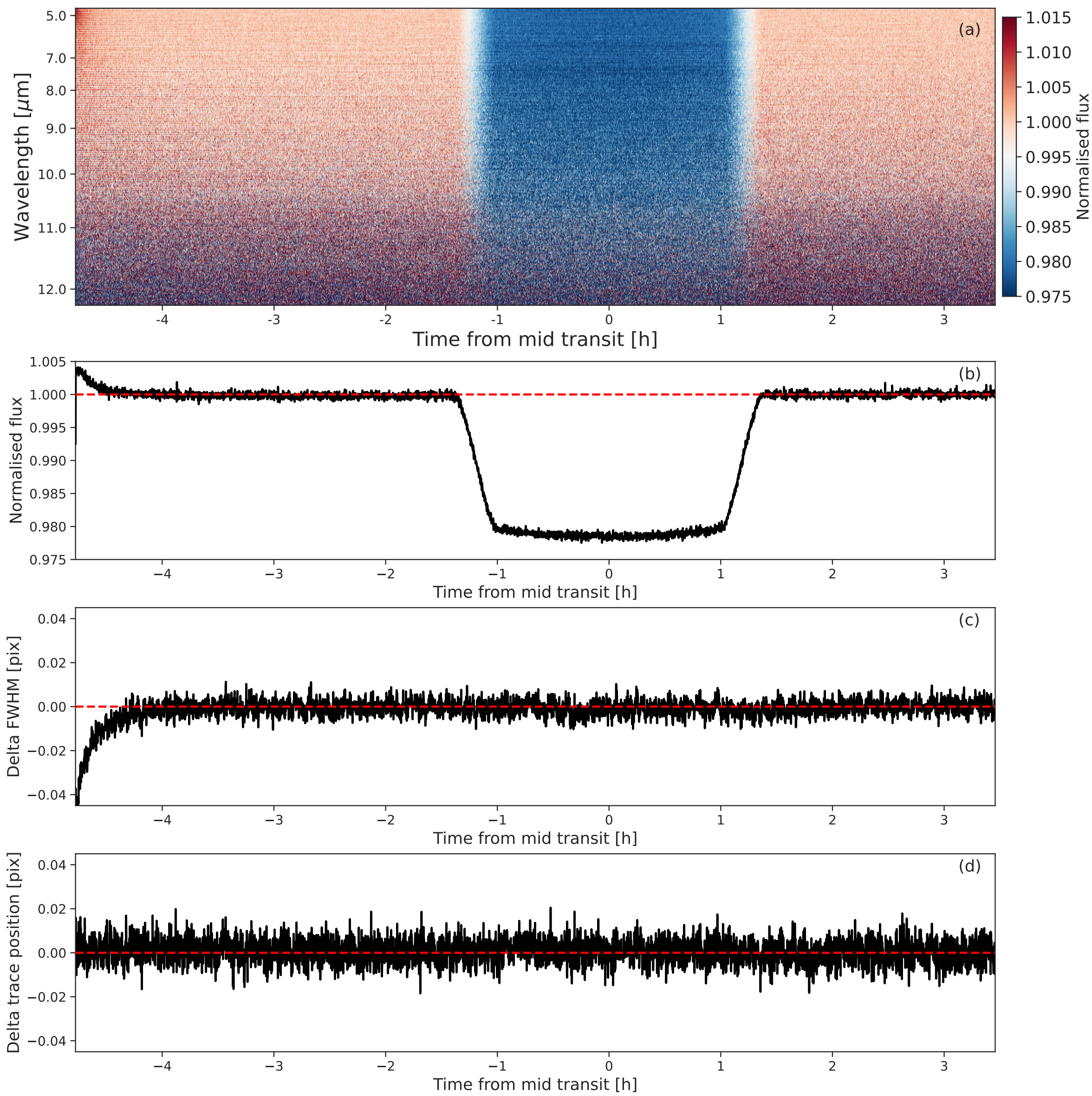


Suppl. Inf. – Figure 1: **Band-average time series of the JWST MIRI/LRS observations of the WASP-107b transit.** Panel (a): Normalised spectral time series data. Panel (b): Normalised light curve of the WASP-107b transit integrated between 4.61 $\mu$m to 11.83 $\mu$m. Panel (c): Change in full-width half maximum (FWHM) in the spectral trace between detector rows 280 and 390, corresponding to the shortest wavelengths. Panel (d): Change in cross-dispersion position of the spectral trace. The dashed lines are drawn to indicate the value to expect in case of no variations in values of the plotted data.

detector in the specific regions differently[40], and could create calibration offsets and extra noise. However, we find no such effects in our data.

Each spectroscopic light-curve as well as the band-averaged light-curve were fitted by a transit model. We fixed the orbital period $\mathrm{P} = 5.7214$ days [1] and derived the semi-major axis, inclination and mid-transit time from fitting the band-averaged light curve. The free parameters for the spectral light curve fitting were the ratio of the planet radius over the stellar radius, $R_p/R_\star$, the instrumental systematics parameters and the limb-darkening coefficients. The transit ephemeris were taken from ref. [42], other system parameters from ref. [43], and quadratic limb-darkening coefficients computed with the `ExoTETHyS` package [44], using the parameterised quadratic parameters from ref. [45]. The parameters retrieved from the band-averaged light curve fitting are presented in Suppl. Inf. Table 1.

Suppl. Inf. – Table 1: **Parameters retrieved from the band-averaged light curve fitting.** Listed are the values retrieved with the `Eureka!` and `TEATRO` reduction methods. `CASCADe` uses the `TEATRO` output parameters. The mid-transit timing $T_0$ is the Barycentric Modified Julian date / Temps Dynamique Barycentrique (BMJD_TDB) time system.

| Parameter | `Eureka!` | `TEATRO` |
|---|---|---|
| Orbital period [d] | $5.7214742$ [(a)] | $5.7214904$ [(b)] |
| Planetary radius $R_p$ $[R_\star]$ | $0.14336^{+6.55154\times10^{-5}}_{-6.75549\times10^{-5}}$ | $0.14341 \pm 0.00011$ |
| Semi-major axis $a$ $[R_\star]$ | $18.10815^{+0.00710}_{-0.00712}$ | $18.0249$ [(c)] |
| Inclination $i$ [deg] | $89.59059^{+0.00837}_{-0.00851}$ | $89.516 \pm 0.016$ |
| Mid-transit timing $T_0$ [d] | $59963.9687968^{+1.30\times10^{-5}}_{-1.27\times10^{-5}}$ | $59963.968763 \pm 1.6 \times 10^{-5}$ |
| Limb-darkening coefficient $u_1$ | $0.095^{+0.0017}_{-0.0015}$ | $0.089 \pm 0.014$ |
| Limb-darkening coefficient $u_2$ | $0.017^{+0.059}_{-0.053}$ | $0.042 \pm 0.029$ |

[(a)] Fixed[2].
[(b)] Fixed[42].
[(c)] Fixed, computed from the orbital period[42] and the stellar mass and radius[1].

### 1.1. CASCADe data reduction setup

The first method for spectral extraction and time series analysis was based on the Calibration of trAnsit Spectroscopy using CAusal Data (`CASCADe`) data reduction package developed within the *Exoplanet Atmosphere New Emission Transmission Spectra Analysis* (`ExoplANETS-A`) Horizon-2020 program and described in detail in ref. [11]. For the basic data calibration and spectral extraction, we used the `jwst` calibration pipeline version 1.9.4 and reference files from the JWST Calibration Reference Data System (CRDS) using context 1030. We followed the procedure described in ref. [11] with a few exceptions. We found that the dark correction applied in context version 1030 was not optimal, as it introduced an excess scatter on the detector ramps. We, therefore, overrode the dark reference file with a custom one, which we derived by taking the standard CRDS dark file and running a median smoothing (or running median) to remove the observed excess scatter in the dark estimate. For a complete discussion on our linearity correction we refer to Sect. 1.4. Secondly, we used the reset switch charge decay (RSCD) step in the Detector1 pipeline stage that flags the first 4 groups of each integration as 'do not use'. Though this decreases the effective integration time, the linearity and stability of the detector signals are improved in a substantial way, resulting in increased signal-to-noise ratios of the final extracted spectra. Note that also the last group of each integration is standard flagged as 'do not use', as this group is strongly affected by the detector reset (see also ref. [47]). The infrared background emission was removed by determining a median background per detector row and integration using detector columns 12 to 19 (starting from 0) and 52 to 59. We used the `CASCADe-filtering` package version 1.0.2 to identify any bad pixels or cosmic ray hits not identified in the Detector1 pipeline stage. We then used this package to clean all pixels flagged as 'do not use' before spectral extraction. We used the `CASCADe-jitter` package version 0.9.5 to determine the spectral trace to be able to precisely position the extraction aperture. The time averaged polynomial coefficients of the spectral trace are $35.29$, $4.313 \times 10^{-3}$, $5.947 \times 10^{-6}$ and $-9.484 \times 10^{-8}$ from zero to third order, respectively. We extracted the 1D spectral time series data from the spectral images using the `extract1d` pipeline step. In this step we used the polynomial coefficients from the trace fit listed above to centre a constant width extraction aperture of 8 pixels at the exact source position for all wavelengths. The spectral flux values are calculated by summing the signal on the detector within the region defined by the extraction aperture and wavelength bins. Suppl. Inf. Figure 1 shows the time series of the extracted LRS spectra. Also shown in that figure is the derived movement of the spectral trace in the cross dispersion direction and the full-width at half maximum (FWHM) of the spectral trace at the shortest wavelengths. Apart from the first half an hour, no substantial photometric or positional drifts can be observed, showing the exquisite stability of the MIRI instrument.

For the light curve fitting, we used the identical procedure as described in ref. [11] using the `CASCADe`-package version 1.2.2. We omitted the first 744 integrations (about 1.3 hours) to avoid the response drifts seen in Suppl. Inf. Figure 1. Before the spectral light curve fitting, we binned the spectra to a uniform wavelength grid with a 0.15 $\mu$m bin width. For the systematics model (see ref. [48] for details), we used as additional regression parameters the time, the FWHM of the spectral trace, and the trace position as plotted in Suppl. Inf. Figure 1. The orbital parameters of WASP-107b were fixed to the values derived in the band-averaged light curve analysis from the `TEATRO` data reduction (see Suppl. Inf. Table 1). Limb-darkening coefficients for each spectral channel were calculated using the `ExoTETHyS`-package [44] (see Suppl. Inf. Table 1). The `CASCADe` band-averaged results from our spectral light curve analysis are presented in Suppl. Inf. Figure 2 and the `CASCADe` transmission spectroscopy results are provided in Extended Data Table 1 and shown in Figure 1. The error estimates on the transit depths were derived by performing a bootstrap analysis.

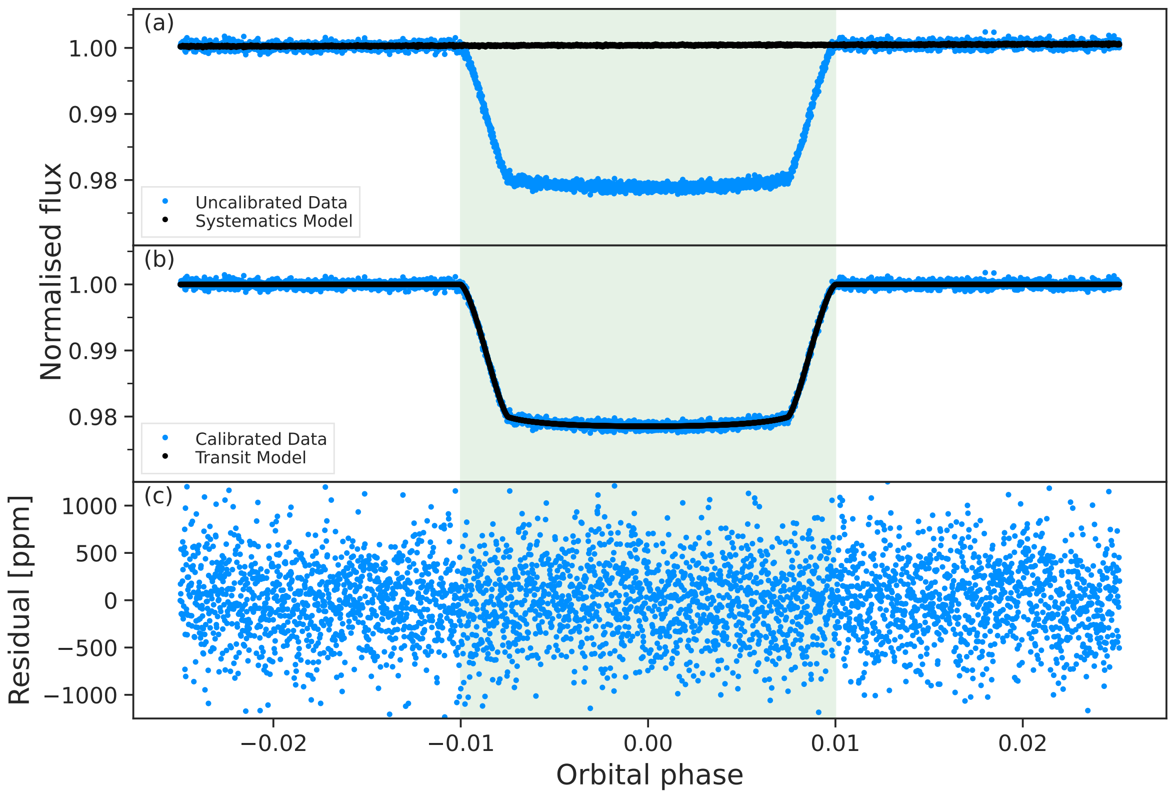


Suppl. Inf. – Figure 2: **`CASCADe` band average light curve analysis.** Panel (a): The band-averaged JWST MIRI/LRS light curve data of the transit of WASP-107b and the fitted systematics model. Panel (b): The systematics corrected band-averaged light curve with the fitted transit model. Panel (c): The band-averaged residuals after subtracting the best-fit light curve model. The shaded area indicates the orbital phases during which the transit occurs. Note that the first 744 integrations have been removed from the light curves shown in this figure.

## 1.2. Eureka! data reduction setup

Data reduction was conducted using the STScI `jwst` pipeline version 1.8.5 under CRDS context 1030. At the ramp and pixel scale, the first four frames corresponding to the ones affected by the RSCD effect[49] were flagged and ramp non-linearity correction was performed using a custom correction file ( Suppl. Inf. 1.4). Contrary to the *CASCADe* and *TEATRO* data reductions, no custom dark file is needed as pipeline version 1.8.5 uses different correction which did not show an excess scatter. Cosmic rays were flagged with a rejection threshold of $5\sigma$ and the ramps were fitted using a least-squared minimisation algorithm. To comply with the JWST MIRI spectroscopic performances of time-series observations[11], the electronic gain value was lowered from 5.5 to 3.1 $e^{-}$ $DN^{-1}$. The background was subtracted following the same method as in ref. [11]. In particular, 7 columns on the left and 7 on the right sides of the trace (column 36) were selected, a median value was taken and then subtracted from the spectral image. A spatial filter of outlier detection was then applied to remove any hot pixel that would have been left in the subarray. An optimal spectral extraction with a half-width extraction aperture of 4 pixels was then performed using the `Eureka!` package [12]. We extracted 51 spectroscopic light curves between 4.61 and 11.83 $\mu$m with a 0.15 $\mu$m bin width, ran a sigma-clipping of 20 integrations with a rejection threshold of $5\sigma$, and trimmed the 250 first integrations to get rid of strong persistence effects. Light curves were then fitted using the MCMC `emcee` sampler [50], the `batman` transit model [51] and both an exponential and a second order polynomial model for systematics. We used the band-averaged light curve fit to refine the mid-transit timing, the ratio of the semi-major axis over the stellar radius, and inclination parameters (see Suppl. Inf. Table 1). The ratio of the planet radius over the stellar radius, the limb-darkening coefficients and the systematics parameters were then used as free parameters for all spectroscopic channels (see Suppl. Inf. Table 1). The `Eureka!` transmission spectroscopy results are provided in Extended Data Table 1 and shown in Figure 1.

### 1.3. TEATRO data reduction setup

We processed the data using the Transiting Exoplanet Atmosphere Tool for Reduction of Observations (`TEATRO`) that runs the `jwst` package, extracts and cleans the stellar spectra and light curves, and runs light curve fits. In the `jwst` Detector1 pipeline, we use the same dark and linearity corrections as in `CASCADe` by overriding the default reference files. We subtracted the background per integration and per detector row and corrected for flagged pixels. We extracted the stellar spectra by summing the flux in a 12 pixel wide aperture, summed them between 4.61 – 11.83 $\mu$m to obtain the band-averaged light flux, and binned them in 51 wavelength bins from 4.61 to 11.83 $\mu$m (bin width of 0.15 $\mu$m) to obtain the spectroscopic light curves. We discarded the first 1.4 hr that show a decay caused by persistence effects, normalised the light curves by the out-of-transit flux, and removed outliers. We fitted the light curves by a transit light curve model computed with the `exoplanet` package [52,53] and a linear trend. We fitted that model to the data using a MCMC procedure based on the `PyMC3` package as implemented in `exoplanet` [52,53]. We refined the mid-transit time, planet-to-star radius ratio, and inclination from a band-averaged light curve fit (Suppl. Inf. Table 1), and let only the planet-to-star radius ratio and a linear trend as free parameters for the spectroscopic light curve fits. The limb-darkening coefficients for each spectral channel were fixed to the values used in the `CASCADe` reduction. We used the median of the posterior distributions as final parameters, and computed the transit depth uncertainties by a quadratic sum of the standard deviations of the residuals of the in- and out-of-transit points divided by the square root of their respective number of points, because it gives more conservative uncertainties than those obtained from the MCMC posterior distributions. The `TEATRO` transmission spectroscopy results are provided in Extended Data Table 1 and shown in Figure 1.

### 1.4. Data non-linearity correction

The adopted readout pattern for all JWST instruments, including those of the MIRI instrument, is the so-called `MULTIACCUM` readout pattern. The MIRI pixels are read non-destructively (charges are read but not reset) at a constant rate until a final read followed by two resets to clear the accumulated charges. An integration thus consists of a number of samples of the accumulating detector signal, resulting in a ramp, that, when fitted, yields a measure of the flux per pixel. For a detailed discussion of the MIRI focal plane arrays and read out patterns we refer to ref. [37].

The MIRI detector ramps show several non-ideal behaviours, influencing the slope derivation and thus the flux estimates. We refer to ref. [47] for a review of all detector effects influencing the sampling of the detector ramps and their mitigation in the JWST data reduction pipeline. The two main non-linearity effects which are important for transit observations are the reset switch charge decay [47] and the debiasing effect in combination with a diffusion of electrons to neighbouring pixels [47,54]. While the former affects mainly the first few reads of the detector ramps, and can be mitigated by not using the affected reads when determining the slope of the detector ramps, the latter effects need to be corrected before the slope of the detector ramps can be correctly measured. For a detailed discussion on the detector voltage debiasing and related effects, see ref. [54]. In brief, a detector circuit as used in MIRI can be seen as a resistor-capacitor circuit. Charge accumulation at the integration capacitors reduces the net bias voltage, which in turn leads to a lower response of the detector as it causes the width of the depletion region to shrink below the active layer width, and a smaller fraction of the produced photoelectrons are guided to the pixels. The diffusion of photo-excited electrons in the undepleted region of a (near) saturated pixel to the depleted region at neighbouring pixels – dubbed the brighter-fatter effect [54] – can be observed in the WASP-107b data but only at a low level, as the maximum observed signal level of the detector ramps remains well below the saturation limit. The main effect of the electron diffusion in the WASP-107b data is an additional loss of electrons in the central pixels of the spectral point spread function (PSF), in combination with a small gain of electrons in the neighbouring pixels in the wing of the PSF. **As we will show in the following, parametric model can still be used for this data set to derive an *effective* debiasing of the detector pixels and properly linearize the detector ramps, mitigating the combined effects of detector debiasing plus electron diffusion.** We, therefore, ignored the electron diffusion effect in our analysis, and focused on correcting the main detector ramp non-linearity due to debiasing.

The standard correction for the non-linearity of the detector ramps due to the debiasing effect, implemented in the `linearity` step of the JWST data reduction pipeline, is derived by fitting a cubic polynomial to the detector ramps of dedicated calibration data, and using the linear term as an estimate of the linearised signal of the detector ramp. A functional relation is then determined between linearised signal and observed signal using a fourth-order polynomial. The polynomial coefficients from this fit are stored in the CRDS calibration file for the `linearity` pipeline step. Note that the standard linearity correction implements an identical correction for all detector pixels in the MIRI/LRS subarray. Also note that the standard correction was derived using data from an spatially extended illumination source, which results in data not influenced by electron diffusion as there is no significant electrical field differences between neighbouring pixels.

To test the default linearity correction (pmap version 1030), we checked the behaviour of the detector ramps by creating pair-wise differences of the readouts (frames or groups in case of

MIRI). In case of a perfect linear ramp, the pair-wise differences of a detector ramp for a single detector pixel should have a constant value. Panels a, d, g, j and m (the left column) of Suppl. Inf. Figure 3 displays the pair-wise differences of the uncalibrated data (`uncal` data product), clearly showing non-constant values for those pixels receiving the highest photon flux. Note that the slope change of the first few differences is dominated by the RSCD, and the last pair by the last-frame effect. Applying the default linearity correction substantially improves the linearity of the ramps but a slope can still be seen when plotting the pair-wise differences in panels b, e, h, k and n (the second column ) of Suppl. Inf. Figure 3, indicating that the default correction is not yet optimal. As non-linearity effects can have a substantial impact on the derived transit depth, we derived an alternative linearity correction based on the data itself. We fitted the following **parametric model** to the detector ramps

$$\mathrm{S_{ij}}(t) = a_{ij,0} + \tau_{ik,1} \cdot a_{ij,1} \cdot \left(1 - \mathrm{e}^{\frac{-t}{\tau_{ij,1}}}\right) - \tau_{ij,2} \cdot a_{ij,2} \cdot \mathrm{e}^{\frac{-t}{\tau_{ij,2}}}$$
$$i \in \{0, \ldots, 415\}, \quad j \in \{0, \ldots, 72\}, \quad 0 \leq t \leq \mathrm{T_{int}}$$

In this equation, $t$ is the time between $0$ and the duration of a single integration $\mathrm{T_{int}}$. The first term represents the debiasing effect, with $a_{ij,0}$ the reset level for a single pixel with detector row index $i$ and column index $j$, $a_{ij,1}$ and $\tau_{ik,1}$ the linearised slope of the detector ramp and **the time constant combined effects of the detector debiasing plus electron diffusion**, respectively. The second term models the RSCD effects with $a_{ij,2}$ and $\tau_{ij,2}$ the amplitude and time constant for the estimate of the RSCD effect. Though we will not use the fitted contribution of the RSCD effect in this study, we included the term in the fit to ensure we obtained an unbiased estimate of the **combined debiasing and electron diffusion effects**. Using this model, we fitted the detector ramps after applying the `reset` pipeline step, for all integrations after the transit. Using the fitted estimate of the linearised signal, we followed the procedure described in ref. [47] to derive a custom non-linearity correction used in the `linearity` pipeline step. Panels c, f, i, l and o (the right column) of Suppl. Inf. Figure 3 show the slope estimates of the linearised ramps using our custom non-linearity procedure. One can see that our custom linearisation improves the linearity of the detector pixels in the detector column at the centre of the spectral trace. To check the linearisation in the of the detector signals in the direction across the spectral trace, we show in Suppl. Inf. Figure 4 our results for several detector columns across the spectral PSF for detector row 385, which corresponds to the shortest wavelengths in our spectra. Comparing our results shown in this latter figure to the linearised ramps using the standard calibration, one can observe again a substantial improvement in the linearity of the ramps. Note that for detector pixels with a row number below 305 (equivalent to wavelengths beyond approximately 8 $\mu$m), which see a sufficiently low signal, no differences can be observed between our calibration and the standard CRDS linearisation. This is expected, as the detector ramps for those pixels are expected to be (near) linear.

Another test to check the non-linearity correction of the detector ramps is to look at the FWHM of the spectral trace. As the central detector pixels in the spectral trace see a stronger signal,

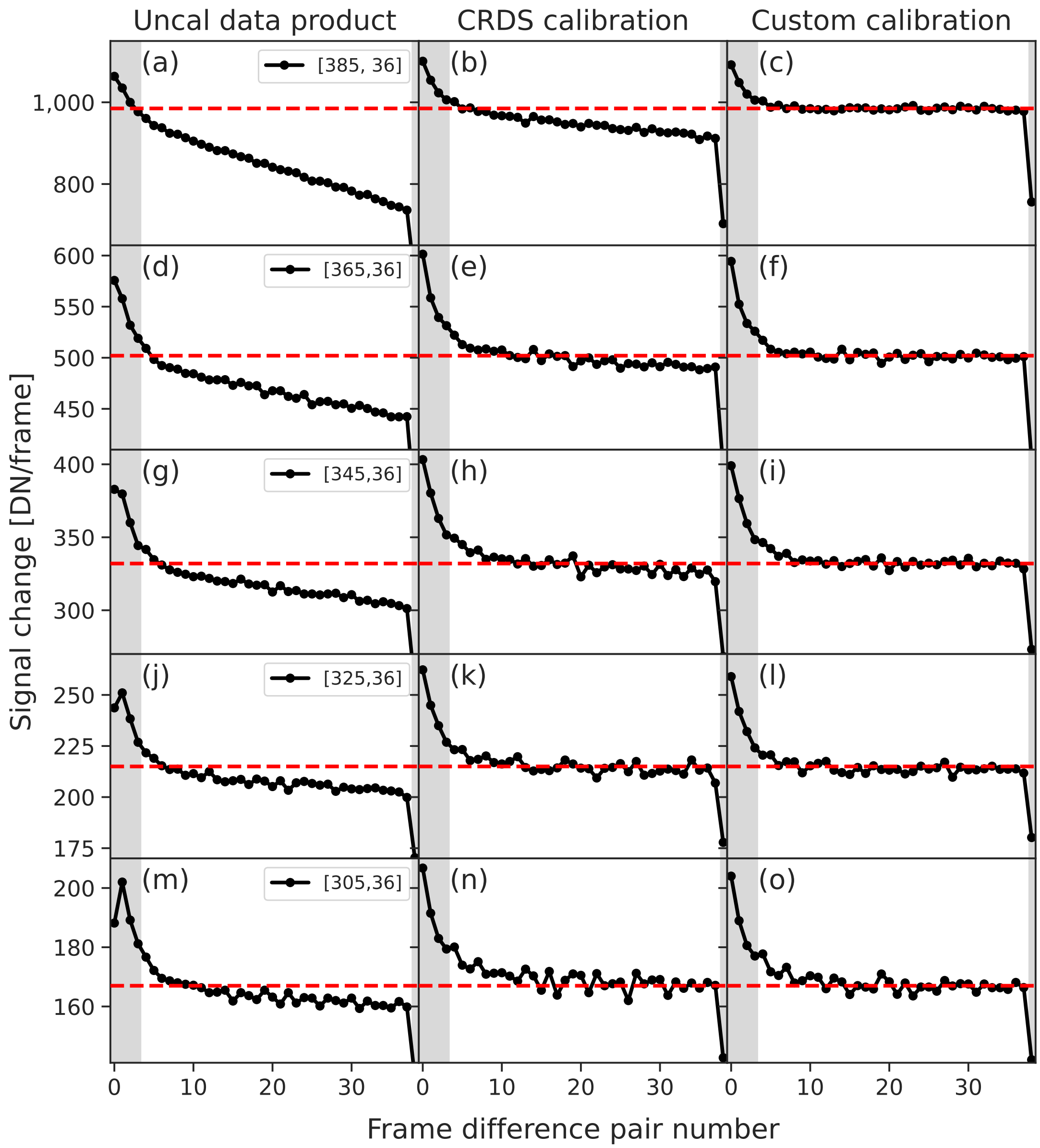


Suppl. Inf. – Figure 3: **Linearity of the detector ramps for selected detector pixels along the spectral trace.** Shown are the pair-wise differences of the samples of the detector ramps for a number of detector pixels. From left to right are shown the ramp gradients for the `uncal` data product, the standard `reset`, `dark` and `linearise` processed data using the calibration files from CRDS with pmap version 1030, and the data product using a custom calibration for the `linearise` and `dark` calibration steps. From top to bottom are shown the data for 5 detector pixels corresponding to the maximum signal in the spectral trace of WASP-107 at different wavelengths. The pixel indices are indicated in the legends shown in the left column. The shaded regions indicate the data not used in the final determination of the slopes of the detector ramps. The dashed lines are plotted to guide the eye and represent the average linear slope after applying our custom calibration.

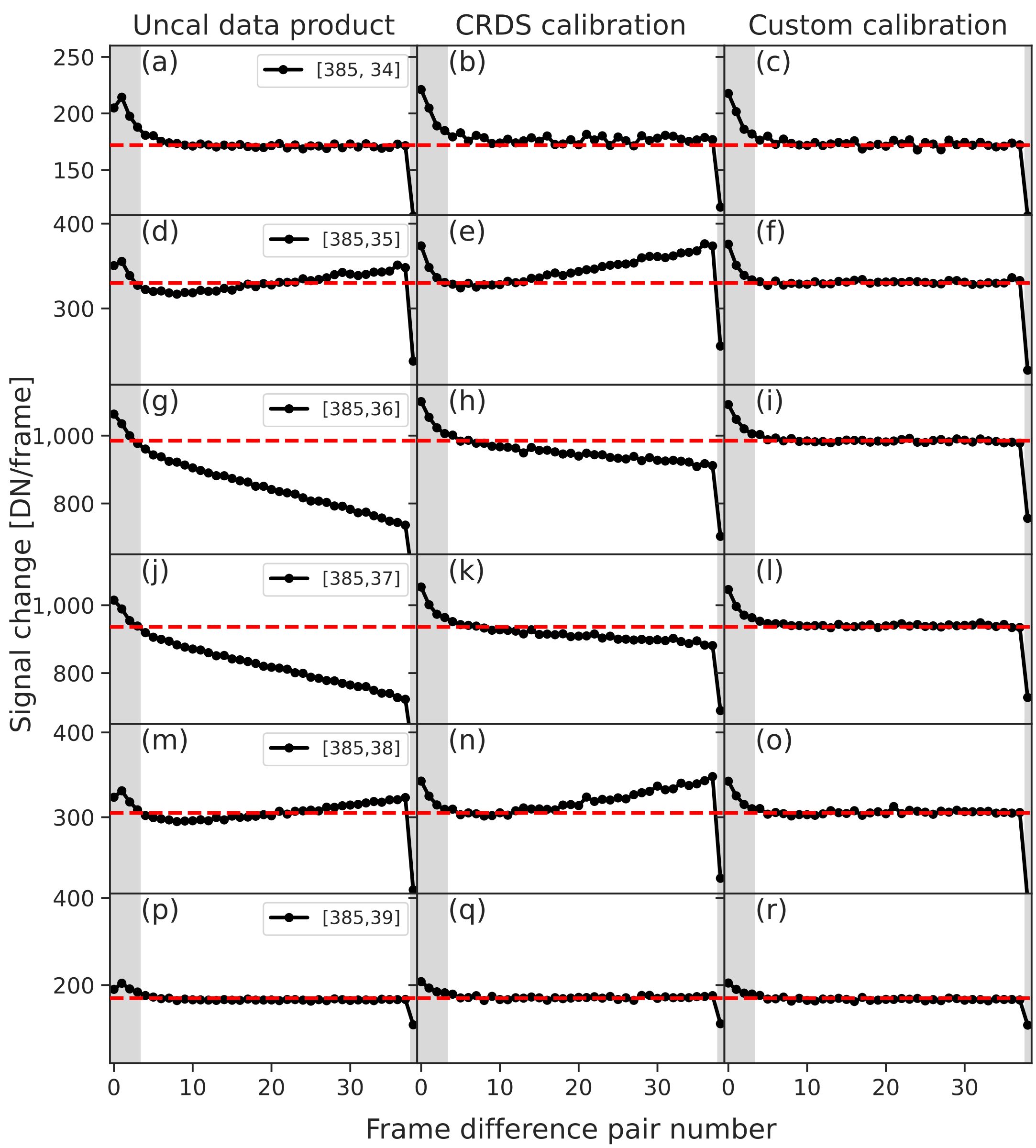


Suppl. Inf. – Figure 4: **Linearity of the detector ramps for selected pixels across the spectral trace.** The data shown in this figure is similar to Suppl. Inf. Figure 3 but now for 6 detector pixels corresponding to a cross-section (from top to bottom, detector columns 34 to 39) of the spectral trace of the dispersed light at detector row 385, the latter corresponding to the shortest wavelength in our spectra. Note that panels g,h,and i correspond to panels a,b, and c of Suppl. Inf. Figure 3.

they will be subject to a stronger non-linearity, leading to a broadening of the point spread function of the individual readouts of the detector ramps during an integration [54]. Suppl. Inf. Figure 5 shows our estimates of the FWHM of the spectral trace for frame difference pairs along the detector ramp. Panels (a) and (c) show the average FWHM of the spectral trace for frame difference pairs 5 to 10, which are the first samples not substantially influenced by the RSCD effects, and the frame difference pairs 34 to 38, respectively. The data calibrated using the standard calibration (panel (a)) clearly shows a broadening of the point spread function (PSF) during an integration. The custom calibrated data, however, shows no such effect (lower left panels). Panels (b) and (d) of Suppl. Inf. Figure 5 show the average FWHM as a function of frame difference pair for the detector rows 382 to 386, which sample the shortest wavelengths and receive the highest photon flux from the target. Again, the detector data calibrated with the standard calibration shows a broadening of the PSF during the sampling up the ramp (panel (b)) while no such effect can be observed for the data calibrated with our custom calibration (panel (d)). The shaded grey regions in the right panels indicate the data not used in the final determination of the slopes of the detector ramps, as those points are strongly affected by the RSCD and last-frame effects.

Finally, Suppl. Inf. Figure 6 shows the FWHM of the brightest pixels as a function of time. As evident in that figure, the data calibrated using the standard CRDS calibration shows a drop of the derived FWHM during the transit. The drop in the observed signal during the transit of about 2% is clearly enough to have a measurable effect on the photometric signal in case the non-linearity of the detector ramps is not properly corrected. Applying our custom calibration for this dataset, no significant effect of the transit on the FWHM estimate can be observed.

### 1.5. Comparison between the three JWST MIRI data reduction setups

To assess the quality of our data reductions and to identify possible biases between the 3 applied data reduction packages, we compared the uncertainty estimates and the differences in the derived transit depths.

We found that with a single-transit observation we reached a spectrophotometric precision of ∼80 ppm in the $7-8\,\mu$m range at a spectral resolution $R=50$ (see Suppl. Inf. Figure 7). We used the JWST Exposure Time Calculator (ETC) [55] to estimate the signal-to-noise ratio on a single integration. Using this estimate, we simulated the light curves per spectral channel assuming a constant transit depth equal to the observed band-averaged transit depth. The simulated light curves were then fitted using the `CASCADe` package to estimate the error of the simulated transit spectrum. This estimate is shown as the solid curve in Extended Data Figure 7. All three data reductions are consistent with this estimate, indicating that our results are close to the photon noise limit of the instrument. Note that the noise limit estimate based on the ETC still contains uncertainties about the exact value of the detector gain and thus photon conversion efficiency and the level and modelling of the infrared background at longer wavelengths. The largest differences between the error estimates are observed at wavelengths beyond 10 $\mu$m, which is expected as the signal to noise of the data rapidly drops beyond this wavelength.

Our derived band-averaged transit depths are 20,463 $\pm$ 39 ppm (see also Figure 1), 20,552 $\pm$ 17 ppm, and 20,566 $\pm$ 33 ppm, for `CASCADe`, `Eureka!`, and `TEATRO`, respectively. These values are within $1\sigma$ of the previously measured transit depth at near-infrared wavelengths with

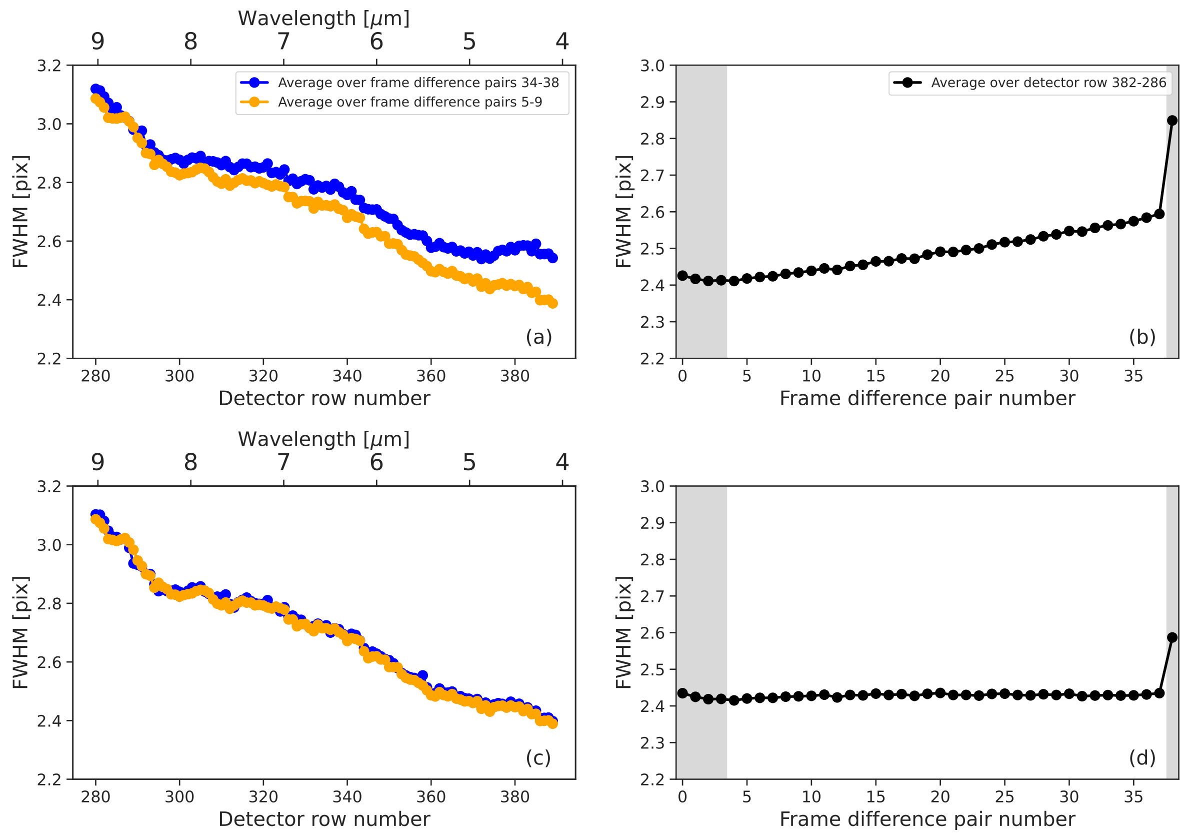


Suppl. Inf. – Figure 5: **FWHM estimates of the spectral trace for different detector ramp frames.** Panels (a) and (b) show the results for the standard calibrated detector ramps while panels (c) and (d) show the results from our custom calibrated data. Panels (a) and (c) show the average FWHM of the spectral trace for detector rows 280 to 390, for frame difference pairs 5 to 10, and 34 to 38, respectively. Panels (b) and (d) show the average FWHM as a function of frame difference pair number for detector rows with the highest signal. The shaded regions in the right panels indicate the data not used in the final determination of the slopes of the detector ramps.

the HST (see Sect. 2.3), and well within $3\sigma$ from each other, showing that all 3 methods give a consistent estimate of the overall transit depth.

For the comparison of the 3 derived transit spectra, we calculated the difference between pairs of data using a different reduction method as

$$\frac{\mathrm{TD}_1(\lambda) - \mathrm{TD}_2(\lambda)}{\sqrt{\mathrm{err}_1^2(\lambda) + \mathrm{err}_2^2(\lambda)}}, \tag{1}$$

with $\mathrm{TD}_1$ and $\mathrm{TD}_2$ being the transit depth of reduction method 1, or 2, respectively, at wavelength $\lambda$ and $\mathrm{err}_1$ and $\mathrm{err}_2$ being the corresponding $1\sigma$ errors shown in Suppl. Inf. Figure 7. As can be seen in Suppl. Inf. Figure 8, the three data reduction methods are within $3\sigma$ agreement, 96% of

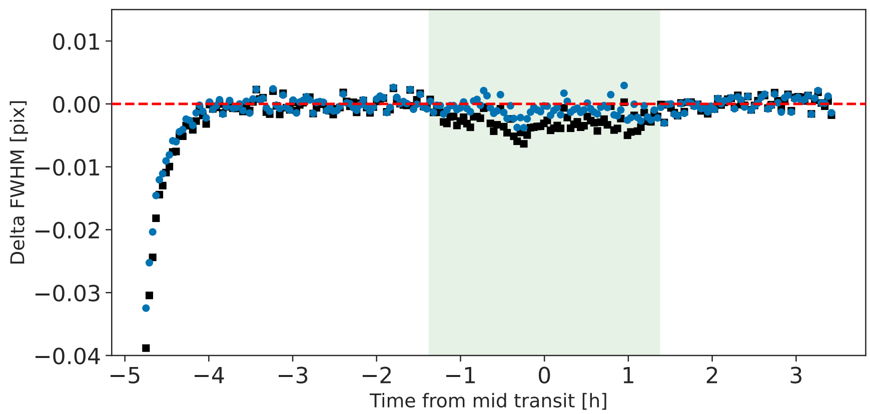


Suppl. Inf. – Figure 6: **Mean FWHM of the spectral trace for the detector rows 380 to 390.** The blue squares show the FWHM as a function of time after applying the standard calibration from CRDS, while the black dots show the measured FWHM after using our custom non-linearity correction. To show the non-linearity effects more clearly, each data point represents an average of 22 integrations. The dashed line is plotted to guide the eye and represents zero variations. The shaded area indicates the time window where the transit occurs.

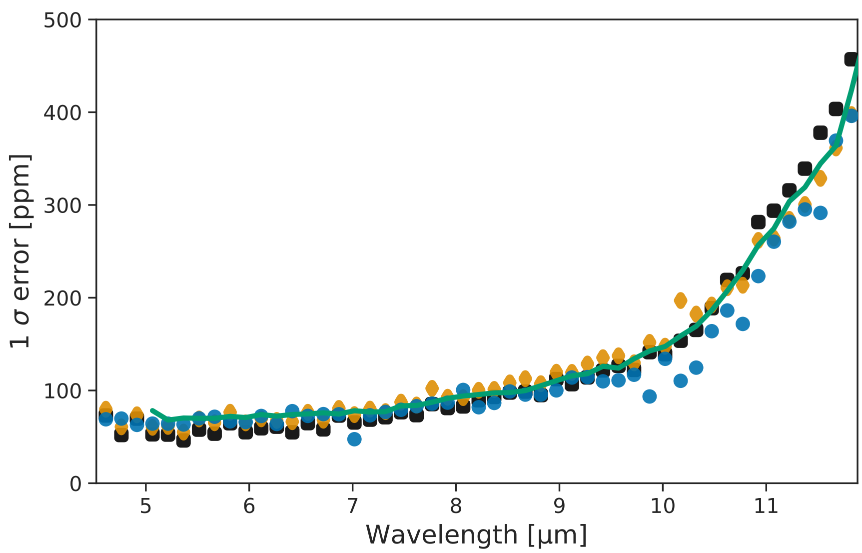


Suppl. Inf. – Figure 7: **1$\sigma$ uncertainties on the transit depths as a function of wavelength for the three data reductions.** The blue dots, orange diamonds and black squares show, respectively, the error estimates using the `CASCADe`, the `Eureka!`, and the `TEATRO` codes. The solid line shows the photon, dark and read noise limited performance estimate based on ETC calculations for comparison. This plot displays the performance of the MIRI/LRS instrument and the reliability of the three data reduction methods.

the points being in $2\sigma$ agreement. For wavelengths shorter than 10 $\mu$m, no significant systematic deviations between the data reductions can be observed. For the longer wavelengths, a small positive offset can be seen in Suppl. Inf. Figure 8 for the three reductions that remains, however, within $1\sigma$ difference.

The observed systematic trend in transit depth differences for the longer wavelengths can be attributed to the different systematics models employed by the `CASCADe`, `TEATRO` and `Eureka!` reduction codes. `TEATRO` cuts the initial ramp caused by persistence effects at the beginning of the observation and fits only a linear trend, `Eureka!` includes both an exponential model at the beginning of the observation and a polynomial one that fits any bending of the light curve, and in the `CASCADe` analysis, the initial response drift caused by persistence effects is also removed and the fitted systematics model is constructed from the data itself (see ref.[56]) using the causal connection between the different wavelength channels in addition to the time, trace position and FWHM. Small differences in the curvature of the baseline will then translate in small differences of the fitted transit depth. **In general, however, these results demonstrate that all three reduction methods are compliant with each other.**

# 2. Ancillary data

## 2.1. NUV data

Contemporaneously with the JWST observations, from 2023 January 5 to 29, *Swift* conducted a 'Target of Opportunity' (ToO) observing campaign (Target Id. 15428) for WASP-107, with the UVOT[57] as the primary instrument, and utilising the uvm2 filter to optimise the waveband definition and avoid redward 'leaks' present in uvw2[58]. The uvm2 filter has a central wavelength of 2246 Å and a FWHM of 498 Å[59]. The observing campaign consisted of 13 *observation segments* comprising a total of 20 *snapshots* (i.e. continuous exposure periods). Each segment was typically $\sim 1.5 – 2$ ks in duration; with snapshots ranging from the full segment length down to $\sim 500$ s. All observations were performed in *full imaging* mode, i.e. the snapshot duration was the maximum available time resolution.

Data from *Swift* observations are automatically processed by the *Swift*-project pipeline, and placed in an online publicly-accessible archive. The required data products, all FITS-format files, were downloaded from the archive, on 2023 February 22. These UVOT data products were, for each of the 13 observation segments, the segment image file summed over the snapshots in the segment (1 or 2 in the present case), the snapshot image file containing the individual snapshot images and the detected sources catalogue table. The photometry presented in the images is in units of recorded counts/pixel, where 1 pixel = $1 \times 1$ arcsec$^2$. The ancillary data and visual inspection of the snapshot-level images, indicated that one snapshot (segment-9, snapshot-1) had an aspect-solution problem. These data were excluded from the associated segment image and from further consideration in our analysis, and had been excluded from the automatic pipeline processing. All the following results reported here were based on the segment-level images, i.e. we have available

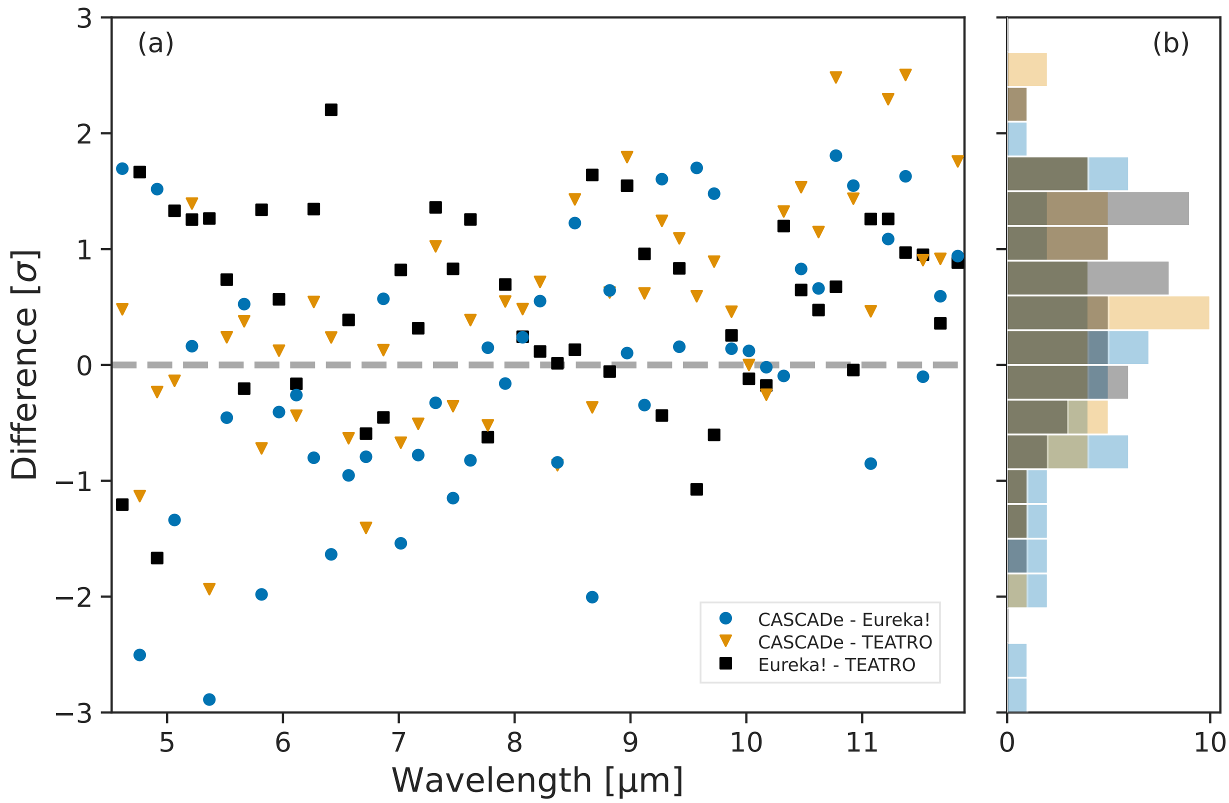


Suppl. Inf. – Figure 8: **Transit depth differences between the three data reduction methods as a function of wavelength.** In panel (a), the blue dots show the differences in units of $\sigma$ between the `CASCADe` and `Eureka!` reductions, the orange triangles the differences between the `CASCADe` and `TEATRO` reductions, and the black squares the differences between the `Eureka!` and `TEATRO` reductions as computed from Eq. 1. The histograms in panel (b) show the number of points in agreement within the different $\sigma$ ranges, with colours identical to those in panel (a).

13 photometry values. We verified that, for the seven segments containing two snapshots, the photometry values were consistent within the statistical errors.

The information in the pipeline-generated source catalogue included, for each detected source, sky-coordinates and photometric values, the latter at successive levels of correction, from 'raw' counts through to PSF-corrected isophotal flux densities. The pipeline source detection employs the *Swift* tool `uvotdetect`, which in turn invokes the SourceExtractor (SE) package [60] to perform source detection and characterisation, including isophotal signal extraction. For WASP-107, we identified, with no ambiguity, the relevant row of the source table based on an estimated epoch=J2023 position using coordinates and proper motions from CDS-SIMBAD. The UV coordinates for all segments lay within 1 arcsec of the estimated optical stellar location and within 0.5 arcsec of the mean UV position. The data were analysed interactively using the *Swift* software tools in HEASoft 6.31.1 and the latest available calibration files (CALDB dated 2021-11-08), with ds9 to display the images, and TOPCAT/STILTS [61] to manipulate and view the source-catalogue tables. As recommended by the *Swift* project, we used the uvotmaghist tool, with a source-data extraction radius of 5 arcsec centred on the mean UV position, to perform aperture photometry for WASP-107 on the 13 segment images. We used an annular background region with the same centre, and inner and outer radii of 20 and 40 arcsec, respectively. We determined by inspection of the UVOT source detections and visually on the images, that the selected background region was free of contamination from nearby sources, and the inner radius was sufficiently removed from the target source to avoid significant contamination.

All 13 aperture-photometry values are consistent within the statistical errors (which dominate the overall errors, as reported by uvotmaghist), with a reduced chi-square $\chi^2/\mathrm{dof} \sim 1$ about the mean (with the degrees of freedom, dof, being 12); and at ∼10%, the sample standard deviation was comparable with the $1\sigma$ error on the individual data values. The source count rate from individual segments was ∼0.1±0.01 ct/s. The mean flux density received at Earth distance was $1.08 \pm 0.03$ erg cm$^{-2}$ s$^{-1}$ Å$^{-1}$, corresponding to a luminosity of $5.4$ erg s$^{-1}$ Å$^{-1}$ and a flux density incident on WASP-107b of $6.4$ erg cm$^{-2}$ s$^{-1}$ Å$^{-1}$. We found good agreement between the flux values from uvotmaghist aperture photometry and uvotdetect/SE isophotal extraction. In making the conversion from instrumental count rate to calibrated flux values, uvotmaghist and uvotdetect assume a gamma-ray-burst-type spectrum, given the prime objective of the mission. However, the difference for a cool-star spectrum is expected to be no more than ∼15% [62]. Given the proximity of WASP-107 to Earth (∼65 pc) and relatively high galactic latitude (∼52 deg), we have not attempted to make any allowance for extinction along the line-of-sight. We note that the NUV irradiance of WASP-107b by its host star is (by chance) comparable (within a factor $\sim 2$) with that of the Earth by the Sun [63], the larger separation of the latter pair being offset by the Sun's hotter and larger-area photosphere (spectral type G2 V versus K6 V).

## 2.2. X-ray data

XMM-Newton has observed the host star WASP-107 on 2018-06-22 (ObsID 0830190901) with the EPIC X-ray telescope (pn, MOS1, MOS2 instruments; all utilising the THIN filter) [64,65] yielding an exposure time of $\sim 60$ ks in a single, continuous observation. The host star was detected in X-rays [66–69], with an X-ray flux in the order of $1 \times 10^{-14}$ erg cm$^{-2}$ s$^{-1}$ in the soft X-rays, equivalent to a luminosity of $\sim (4-7) \times 10^{27}$ erg s$^{-1}$ (depending on the adopted spectral energy range) for a distance of 64.7 pc, yielding an X-ray flux incident on WASP-107b of $\sim 5 \times 10^2$ erg cm$^{-2}$ s$^{-1}$ [68].

The flux and luminosity values in the cited literature have a wide range with differences of up to ∼40%. Therefore, we have performed our own analysis of the XMM-Newton X-ray data, using the SAS data-analysis package, to extract source (and background) counts as a function of photon energy. We binned the spectra to bins with at least 25 source counts each to allow for proper application of $\chi^2$ fit statistics. The source count-rate was ∼0.01 ct/s, and the time-series showed no evidence for variability. The XSPEC package [33] was used for fitting optically-thin thermal models in collisional equilibrium (coronal models) to the extracted spectra, having two temperature components representing a wider, presumably continuous distribution of plasma, and a photoelectric absorption component to account for interstellar absorption. The data from all three EPIC instruments were fitted simultaneously after removing the notoriously difficult lowest-energy spectral bins below 0.2 keV. Following ref.[69], we adopted a fixed, interstellar photoelectric absorption component equivalent to a hydrogen column density of $N_{\mathrm{H}} = 2 \times 10^{19}$ cm$^{-2}$ given the distance to WASP-107.

Owing to the relatively modest signal-to-noise ratio (SNR) of the spectrum, the fits converged to two classes of solutions in very different temperature regimes. We discriminated between them by requiring that the solution fulfils the general scaling law between average X-ray stellar surface flux and the logarithmically averaged coronal temperature, using the emission measures ($\mathrm{EM} = \int n_e n_i \mathrm{d}V$, where $n_e$ and $n_i$ are the coronal electron and ion number densities, respectively, and $V$ is the coronal volume occupied by the plasma) of the components as weights [71].

The coronal abundances are important quantities for such a fit but the limited SNR does not allow individual element abundances to be retrieved. We therefore used one common abundance factor $Z$ for all elements with respect to their solar photospheric values (relative to H). We then stepped through a grid of fixed $Z$ values, fitting the spectrum for each $Z$, and then searching for a solution that fulfils the coronal flux-temperature scaling relation while providing low $\chi^2$ value. Such a solution exists, with a reduced $\chi^2$ value of 0.94 for $Z = 0.22$. The formal best-fit yielded temperatures of $T_1 = 1.69$ MK (million K) and $T_2 = 8.6$ MK, with an emission-measure ratio $\mathrm{EM}_2/\mathrm{EM}_1 = 0.54$. The EM-weighted logarithmic average of the coronal temperatures as defined in ref.[71] $\left(\log \bar{T} = \sum_i \mathrm{EM}_i \log T_i / \sum_i \mathrm{EM}_i\right)$ is $\bar{T} = 2.96$ MK, a relatively modest temperature as expected for a low-activity star. The corresponding absorption-corrected X-ray flux at Earth in the spectral range of 0.1 – 10 keV is $1.76 \times 10^{-14}$ erg cm$^{-2}$ s$^{-1}$, equivalent to a luminosity of $L_{\mathrm{X}} \approx 8.8 \times 10^{27}$ erg s$^{-1}$ for a distance of 64.7 pc, yielding an X-ray flux incident on WASP-107b of $\sim 9.7 \times 10^2$ erg cm$^{-2}$ s$^{-1}$.

A rotation period of $17.5 \pm 1.5$ d was derived from *Kepler* K2 photometry [72], while the WASP-107 photometry yields an estimate of $17 \pm 1$ d [1]. From gyrochronology modelling and the rotation period derived from the WASP photometry, an age estimate of $3.4 \pm 0.3$ Gyr has been derived [2]. From recent studies of the activity-age-rotation relation for cool main-sequence stars[73] we would expect an X-ray luminosity in the order of $10^{28}$ erg s$^{-1}$ for a star with a mass of $0.68\ M_\odot$ and an age of a few Gyr. This matches our derived X-ray luminosity very well.

### 2.3. HST data

A transit of WASP-107b was observed on June 5–6, 2017 with the Wide Field Camera 3 (WFC3) instrument onboard the *Hubble Space Telescope* (HST) using the 1.41 $\mu$m Grism (G141). The data were obtained as part of the general observer program 14915 (P.I. L. Kreidberg). We refer to ref. [4] for details on the observations and the initial data analysis. We performed an independent calibration and light curve fitting of the HST data using the `CASCADe` package. For details on the use of `CASCADe` on HST data, see ref. [48]. We ran `CASCADe` using the same orbital and stellar parameters as used for the analysis of the JWST MIRI light curve data (see Methods), except for the ephemeris, for which we used the value published in ref. [42]. This latter value gives a mid-transit time within 28 s of the value derived by ref. [4]. We choose to use the value of ref. [42] as it resulted in slightly lower residuals after subtracting the best fit light curve model.

Before fitting the spectral light curve data, we binned the original spectral resolution of the HST/WFC3 data to a uniform wavelength grid with a spectral bin width of $0.00757\mu$m. Of the first HST orbit, the first 6 spatial scans were not used in our analysis as they showed a very strong initial drift. For the systematics model (see ref. [48] for details), the additional regression parameters were the time variable and the trace position. The derived transit spectrum is plotted in the top panel of Figure 9 (blue squares). We derived a band-averaged transit depth of 20,448$\pm$79 ppm, consistent within $1\sigma$ of the transit depth derived from the JWST MIRI observations. The errors in the transit spectrum and band-averaged depth were estimated by performing a bootstrap analysis. For the retrieval analysis, we binned the spectrum to a slightly lower spectral resolution, with a spectral bin width of about 0.02 $\mu$m to increase the signal-to-noise ratio per spectral channel and to ensure that each spectral bin is independent. A comparison of the spectrum derived using the `CASCADe` package to the previous published spectrum of ref. [4] can be seen in the lower panel of Suppl. Inf. Figure 9. Both spectra are in excellent agreement with each other. The band-averaged transit depth of ref. [4] is 145 ppm, less than $2\sigma$, larger than the averaged depth we derived. This difference is consistent with the quoted error bars and can easily be explained by the large systematics and sparse time sampling of the data, in combination with the different methods used to fit the baselines of the spectral light curves.

# 3. Retrieval analysis

To constrain the atmospheric properties of WASP-107b we carried out retrievals with two different codes: `ARCiS` [13] (see Sect. 3.1) and `petitRADTRANS` [14] (see Sect. 3.2).

## 3.1. `ARCiS` retrieval setup

The atmospheric modelling and retrieval code `ARCiS` [13] was used to perform retrievals using a free parameterised retrieval setup. Our nominal model for `ARCiS` consists of a pressure-temperature profile with a constant value of $d\log T/d\log P$. The temperature at a pressure level of 1 bar is retrieved. Since this is too deep in the atmosphere to be observable, we report the temperature and uncertainties derived from this profile at $P = 10^{-5}$ bar, which is the pressure level dominating the observed transit spectrum. It is important to realise that the derived temperature gradient is only representative of the uppermost atmosphere that we probe with the observed transit spectrum. We include as absorbing molecular species $H_2O$[77], CO [78], $CO_2$ [79], $CH_4$ [80], $C_2H_2$ [81], $SO_2$ [82], SO [83], $H_2S$ [84], SiO [85], HCN [86], $NH_3$ [87], and $PH_3$ [88]. The temperature and pressure dependent opacities were computed from the line lists and formatted for `ARCiS` input [89]. For each species, a log-uniform prior for the volume mixing ratio from $10^{-12}$ to 1 was taken. The remaining atmosphere consists

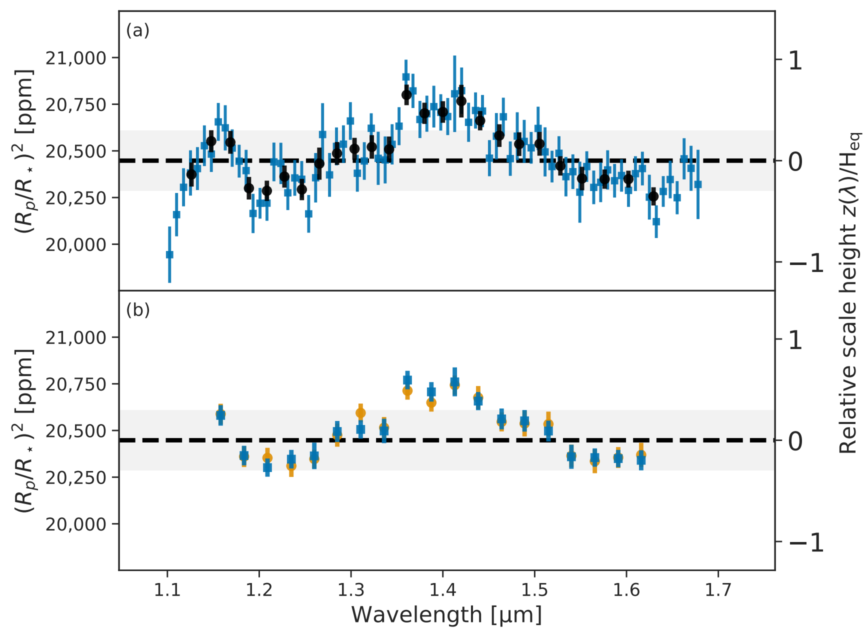


Suppl. Inf. – Figure 9: **HST/WFC3 transmission spectrum of WASP-107b.** Panel (a) shows the transmission spectrum derived using the `CASCADe` package (blue squares) together with a slightly lower resolution version of the same spectrum used in the retrieval analysis (black dots). Panel (b) shows the comparison between the spectrum derived by ref. [4] (green dots) and the `CASCADe` spectrum (blue squares), binned to the published wavelength resolution of ref. [4]. In both panels, the band-averaged transit depth is indicated by the dashed vertical line. The shaded area represents the 95 % confidence interval of the mean transit depth. The right y-axis gives the planetary spectrum in units of atmospheric scale height of the planetary atmosphere assuming it to be hydrogen dominated. In panel (b), the ref. [4] spectrum was shifted downwards by 145 ppm to the same mean transit depth as found in the `CASCADe` analysis for better comparison between the two spectra.

of $H_2$ and He with a number density ratio of 0.85:0.15.

The cloud is modelled as a Gaussian layer with a certain width and optical depth at $9\,\mu$m. The specific cloud density as a function of pressure $P$ is given by

$$f_{\rm cloud} = \frac{g\,\tau_{\rm cloud}}{\kappa_{\rm cloud}\,P\,\sigma_P\sqrt{2\pi}}\exp\left(-\frac{1}{2\sigma_P^2}\left[\log\frac{P}{P_0}\right]^2\right), \tag{2}$$

where $g$ is the gravitational acceleration of the planet, $\kappa_{\rm cloud}$ is the cloud opacity at $9\,\mu$m. The parameters $\tau_{\rm cloud}$ (the cloud optical depth), $P_0$ (the cloud pressure), and $\sigma_P$ (the cloud width) are retrieval parameters. Finally, we consider partial cloud coverage using a retrieval parameter $f_{\rm coverage}$ between zero and one.

For the composition of the cloud particles we take a mixture of amorphous $MgSiO_3$ [90], $SiO_2$ [91–93], SiO [94] and amorphous carbon [95]. We mix the refractive indices of these materials using effective medium theory. We use the standard multi-component Bruggeman mixing rule. This mixing rule has the benefit that all materials are treated the same and there is no dominant matrix material defined (as is the case in the simpler Maxwell-Garnett mixing rule). Note that amorphous carbon provides a continuum opacity and can be considered a placeholder for any cloud component with a featureless spectrum (like, for example, metallic iron). The size of the particles, $a_{\mathrm{cloud}}$, is assumed constant throughout the cloud and the optical properties are computed using irregularly shaped particles simulated by the DHS (Distribution of Hollow Spheres) method [96] where the irregularity parameter $f_{\max}$, which describes how far the particle shape deviates from a homogeneous sphere, is another free parameter. The prior for $a_{\mathrm{cloud}}$ is taken to be $\log$-uniform from 0.01 to 10 $\mu$m. For $f_{\max}$ we take a linear prior from $0$ to $1$.

The above setup has 24 free parameters (1 for the radius, 2 for the $T$-$P$ structure, 12 molecules, and 9 for the cloud structure and particle size/shape). We add one additional parameter allowing for scaling of the HST data with respect to the JWST observations with a 0.38% Gaussian prior corresponding to the uncertainty on the band-averaged transit depth. All parameters and corresponding prior ranges are given in Suppl. Inf. Table 2. In the `ARCiS` retrievals we include the full HST and the MIRI spectrum. In addition to this base model we also perform retrievals where one of the molecular components is removed to test its significance. We convert the natural logarithm of the Bayes factors into a rejection significance using the formalism presented in ref. [97]. To test the significance of the clouds we perform retrievals using no clouds and one where the cloud opacity is replaced with a parameterised opacity. A full corner plot showing the posterior distribution for all retrieval parameters is shown in Suppl. Inf. Figure 10.

### 3.2. `petitRADTRANS` retrieval setup

Our nominal `petitRADTRANS` (`pRT`) forward model assumed an isothermal planetary atmosphere with a uniform prior on temperature from 200 to 2,000 K. The following line absorber species were included: $H_2O$ and CO [78], $C_2H_2$ [81], $CO_2$ [79], $CH_4$ [80], $SO_2$ [82], $H_2S$ [84], SiO [85], HCN [86], $NH_3$ [87] and $PH_3$ [88]. The opacities of all but the first two species were calculated in the `pRT` format by ref. [89]. The mass fractions of all molecules were retrieved freely, with a $\log$-uniform prior from $10^{-10}$ to 1. The remaining atmospheric gas was assumed to be in the form of $H_2$ and He, at a mass ratio of 0.72:0.28. The retrieved molecular mass fractions were converted to volume mixing ratios for comparison with the `ARCiS` results. As gas continuum opacities we considered $H_2$-$H_2$ and $H_2$-He collision induced absorption in addition to $H_2$ and He Rayleigh scattering [98–105]. The planetary gravity was retrieved using tight priors from band-averaged light curve measurements on the planet radius and from radial velocity (RV) measurements on the mass [1]. The planet radius at the reference pressure (taken to be 0.01 bar) was retrieved as a separate free parameter, using a uniform prior from 0.7 to 2 $R_{\mathrm{J}}$. For our 'complex' cloud model we included amorphous $MgSiO_3$ [106], $SiO_2$ [91–93] and crystalline KCl [92] clouds, considering them to be irregularly shaped (DHS method [96]). The cloud mass fractions at the base of the cloud had $\log$-uniform priors from $10^{-10}$ to 1, and the cloud base pressures $P_{\mathrm{base}}$ were retrieved with a $\log$-uniform prior from $10^{-6}$ to 1,000 bar. Above the cloud deck (at lower pressures) the cloud mass fraction was defined as

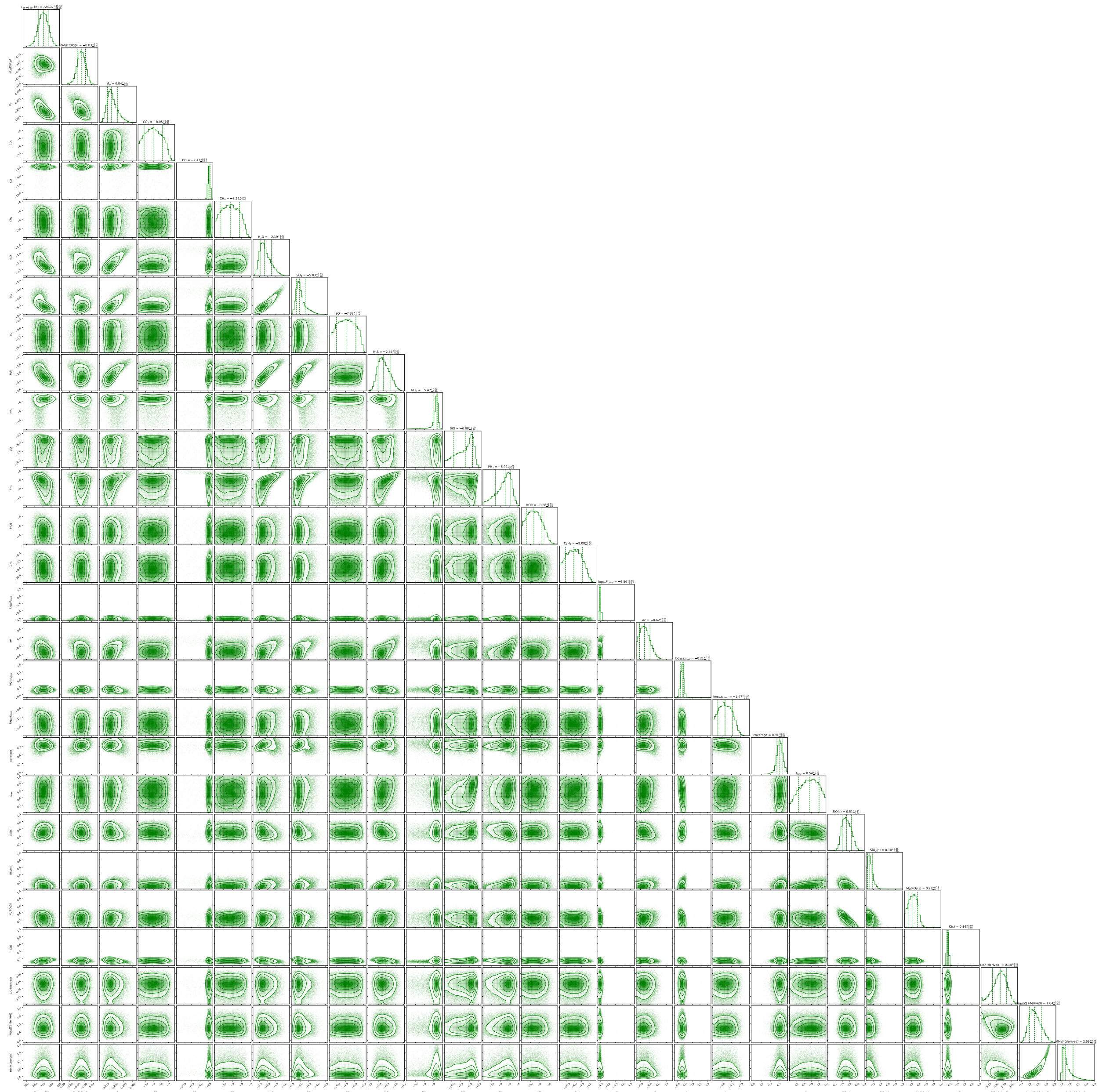

Suppl. Inf. – Figure 10: **Full corner plot for the retrieval of the transit spectrum with the `ARCiS` setup.** The posterior distribution is shown for all retrieval parameters with the addition of the derived parameters metallicity ($Z$), C/O ratio and mean molecular weight (MMW). Gas absorber abundances are shown in logarithms (base 10) of the volume mixing ratios. Note that even though the temperature at 1 bar was retrieved, we present here the posterior of the temperature at $10^{-5}$ bar which is closer to the pressure layers determining the shape of the transit spectrum.

$X_{\rm base}\,(P/P_{\rm base})^{f_{\rm sed}}$, where $X_{\rm base}$ is the mass fraction at the cloud base and $f_{\rm sed}$ is the settling parameter, defined as the cloud particles' mass-averaged ratio of settling and mixing velocities. The prior on $f_{\rm sed}$ was uniform, ranging from 0 to 10. The cloud particle sizes were then found as described in ref. [107], namely by assuming a $\log$-normal size distribution, and making use of $f_{\rm sed}$, $K_{\rm zz}$, and $\sigma_{\rm g}$, where $K_{\rm zz}$ is the vertical eddy diffusion coefficient and $\sigma_{\rm g}$ is the width of the $\log$-normal particle size distribution. We assumed a $\log$-uniform prior from $10^5$ to $10^{13}$ $\rm cm^2\ s^{-1}$ for $K_{\rm zz}$ and a $\log$-uniform prior on $x_\sigma$ from $10^{-2}$ to 1, where $\sigma_{\rm g} = 1 + 2x_\sigma$. For our 'simple' cloud model we replaced the cloud extinction opacity by $\kappa(\lambda, P) = \kappa_{\rm base}\,[1 + (\lambda/\lambda_0)^{-p}]\,(P/P_{\rm base})^{f_{\rm sed}}$, where $f_{\rm sed}$ and $P_{\rm base}$ have the same meaning and priors as before. The opacity at the cloud base was retrieved with a $\log$-uniform prior from $10^{-20}$ to $10^{20}$ $\rm cm^2\ g^{-1}$, $\lambda_0$ with a $\log$-uniform prior from 0.01 to 100 $\mu$m, and $P$ with a uniform prior from 0 to 6. For both forward models we allowed for a multiplicative flux scaling by 0.38% and 0.185% (Gaussian standard deviation of prior), for the HST and JWST data, respectively, corresponding to the uncertainties on the band-averaged transit depths. In the `petitRADTRANS` retrievals we include the full HST spectrum and the MIRI spectrum. All parameters and corresponding prior ranges are given in Suppl. Inf. Table 2. To convert the natural logarithm of the Bayes factors, $\Delta\log(Z)$, into a rejection significance we use the formalism presented in ref. [97]. A full corner plot showing the posterior distribution for all retrieval parameters is shown in Suppl. Inf. Figure 11

### 3.3. Silicate cloud detection significance

In order to determine the significance of the silicate cloud contribution to the retrieval we compare the Bayesian evidence to that of a retrieval performed using a parameterised cloud setup and to a retrieval using an atmospheric setup without clouds. The parameterised cloud setup uses exactly the same cloud structure but a wavelength-dependent opacity characterised by

$$\kappa(\lambda) \propto (1 + (\lambda/\lambda_0)^p)^{-1}, \tag{3}$$

with the two parameters $\lambda_0$ and $p$ being retrieval parameters. Eq. (3) captures the expected behaviour of cloud opacities, being largely constant at short wavelengths (cut-off set by the wavelength $\lambda_0$) and having a slope at large wavelengths (set by the dimensionless parameter $p$). The Bayes factor of the silicate cloud model with respect to the parameterised cloud model tells us if the 10 $\mu$m silicate feature is required to fit the data. The comparison of the silicate cloud model to the model without clouds tells us if clouds are needed at all in the atmosphere. Furthermore, using `ARCiS`, we compare the cloud setup with only a single cloud component. The results are summarised in Suppl. Inf. Table 3. As can be seen, all setups including any silicate component (either SiO, $SiO_2$ or $MgSiO_3$) are preferred over simplified setups. The cloud containing only carbon opacity acts very similar to our parameterised opacity as it only provides a featureless continuum. It is therefore preferred over no clouds but not preferred over the parameterised setup. We also tested the significance of the silicate cloud setup for the other two data reductions, with `TEATRO` and `Eureka!`, and find also these reductions provide strong detections of silicate clouds.

To investigate how sensitive our silicate cloud detection is to specific wavelength regions in

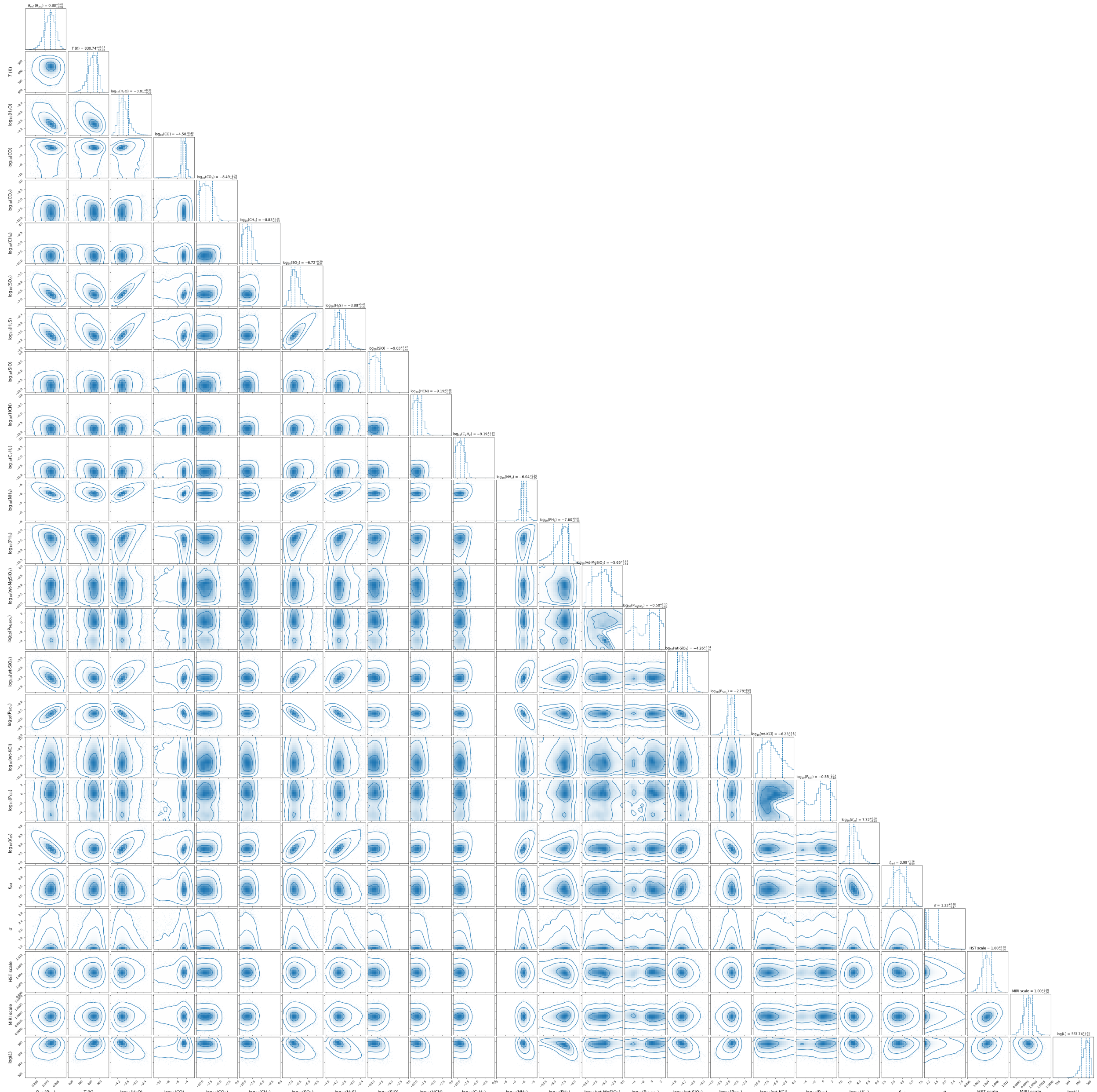

Suppl. Inf. – Figure 11: **Full corner plot for the retrieval of the transit spectrum with the `petitRADTRANS` setup.** The posterior distribution is shown for all retrieval parameters. Gas absorber abundances are shown in logarithms (base 10) of the volume mixing ratios, while the cloud abundance at the cloud deck is given in $\log_{10}$ mass fractions.

the MIRI spectrum, we performed the analysis described above for either the full MIRI wavelength range and additionally using only the MIRI spectrum up to a given wavelength $\lambda_{\rm max}$. With this exercise we aim to establish the robustness of our retrieved cloud setup acknowledging ongoing

Suppl. Inf. – Table 2: **Parameters and prior rages used in the `ARCiS` and `petitRADTRANS` (`pRT`) retrieval analysis.**

| | Prior range | | Prior type |
|---|---|---|---|
| Parameter | `ARCiS` | `pRT` | |
| T at 1 bar [K] | $100 - 2000$ | $200 - 2000$ | linear |
| $d \log T / d \log P$ | $-0.1 - 0.1$ | $0^{(a)}$ | linear |
| $R_p$ [$R_{\rm Jup}$] | $0.7 - 1.14$ | $0.7 - 2.0$ | linear |
| $\log_{10}(g)$ (cgs units) | $2.47^{(a)}$ | $2.43 \pm 0.05$ | Gaussian |
| Molecular abundances | $10^{-12} - 1^{(b)}$ | $10^{-10} - 1^{(c)}$ | logarithmic |
| Cloud properties | | | |
| $P_0$ [bar] | $10^{-5} - 10^{3}$ | - | logarithmic |
| $\sigma_P$ | $0.1 - 10$ | - | logarithmic |
| $\tau_{\rm cloud}$ | $10^{-4} - 10^{3}$ | - | logarithmic |
| $a_{\rm cloud}$[$\mu$m] | $10^{-2} - 10$ | - | logarithmic |
| $f_{\rm max}$ | $0 - 1$ | - | linear |
| Material mass fractions | $0 - 1$ | - | linear |
| $f_{\rm coverage}$ | $0 - 1$ | - | linear |
| $P_{\rm base}$ [bar] per material | - | $10^{-6} - 10^{3}$ | logarithmic |
| $X_{\rm base}$ per material | - | $10^{-10} - 1$ | logarithmic |
| $f_{\rm sed}$ | - | $0 - 10$ | linear |
| $K_{\rm zz}$ [cm$^2$ s$^{-1}$] | - | $10^{5} - 10^{13}$ | logarithmic |
| $x_\sigma$ | - | $10^{-2} - 1$ | logarithmic |

$^{(a)}$ fixed value. $^{(b)}$ volume mixing ratio. $^{(c)}$ mass fraction.

discussions in the community on potential higher systematic errors for MIRI transit depths at longer wavelengths. We emphasise here that in our data we see no indications of any shadowed region that would increase the systematic errors for wavelengths between 10 and $\sim$12 $\mu$m.

It is expected that the significance of the silicate detection drops quickly if we exclude all wavelengths longer than 10 $\mu$m because this is where the silicate feature is present (see Suppl. Inf. Figure 12). In Extended Data Figure 5 we show the resulting detection significance as a function of the maximum wavelength used in the analysis. It is clear that clouds are required no matter what wavelength range we choose. As expected, if we remove the entire wavelength range where the silicate feature is present (so wavelengths above 9.5 $\mu$m) the silicate clouds are no longer detected. In these cases it is seen that the model prefers the setup with fewer parameters, which is the parameterised cloud setup.

Silicate clouds are preferred with a significance of 5.7$\sigma$ even if we remove all MIRI observation with wavelengths longer than 10 $\mu$m. This significance quickly increases if we increase the

Suppl. Inf. – Table 3: **Significance of improvement of the fit with `ARCiS` for various cloud setups with respect to no clouds or with respect to clouds with a parameterised opacity.**

| Setup | CASCADe | TEATRO | Eureka! |
|---|---|---|---|
| With respect to no cloud | | | |
| All cloud components | $9.2\sigma$ | -[a] | -[a] |
| Parameterised opacity | $6.0\sigma$ | -[a] | -[a] |
| Only SiO | $9.7\sigma$ | -[a] | -[a] |
| Only $SiO_2$ | $7.7\sigma$ | -[a] | -[a] |
| Only $MgSiO_3$ | $8.8\sigma$ | -[a] | -[a] |
| Only carbon | $5.8\sigma$ | -[a] | -[a] |
| With respect to a cloud with parameterised opacity | | | |
| All cloud components | $7.2\sigma$ | $7.6\sigma$ | $5.2\sigma$ |
| Only SiO | $7.8\sigma$ | -[a] | -[a] |
| Only $SiO_2$ | $5.1\sigma$ | -[a] | -[a] |
| Only $MgSiO_3$ | $6.6\sigma$ | -[a] | -[a] |
| Only carbon | $-2.2\sigma$ | -[a] | -[a] |

[a] not tested.

maximum wavelength used in the analysis showing that the detection of silicate clouds is a robust result.

# 4. (Photo)chemical models

## 4.1. (Photo)chemical model setup

The goal of the forward (photo)chemical models is to understand the gas-phase formation of molecules in the atmosphere of WASP-107b and to derive the sensitivity of the predicted molar fractions on the model's input parameters. Since the primary focus is on the gas-phase formation of $SO_2$, $CH_4$, and $H_2O$, no cloud-formation processes have been included in these models.

In the case of WASP-107b, a tidally-locked planet with an equilibrium temperature of $\sim$740 K, and orbiting a K6 dwarf host star [2,108], it is anticipated that there will be no significant spatial gradients in the temperature structure and zonal wind speeds [109]. Consequently, we adopt a one-dimensional configuration to examine the chemical abundance distribution within the atmosphere of WASP-107b.

The forward chemical models [110] for WASP-107b were computed considering a host star radius, $R_\star$, of 0.676 $R_\odot$, a planet radius $R_p$ of 0.94 $R_J$, and a planet mass $M_p$ of 30.51 $M_\oplus$ [108]. The

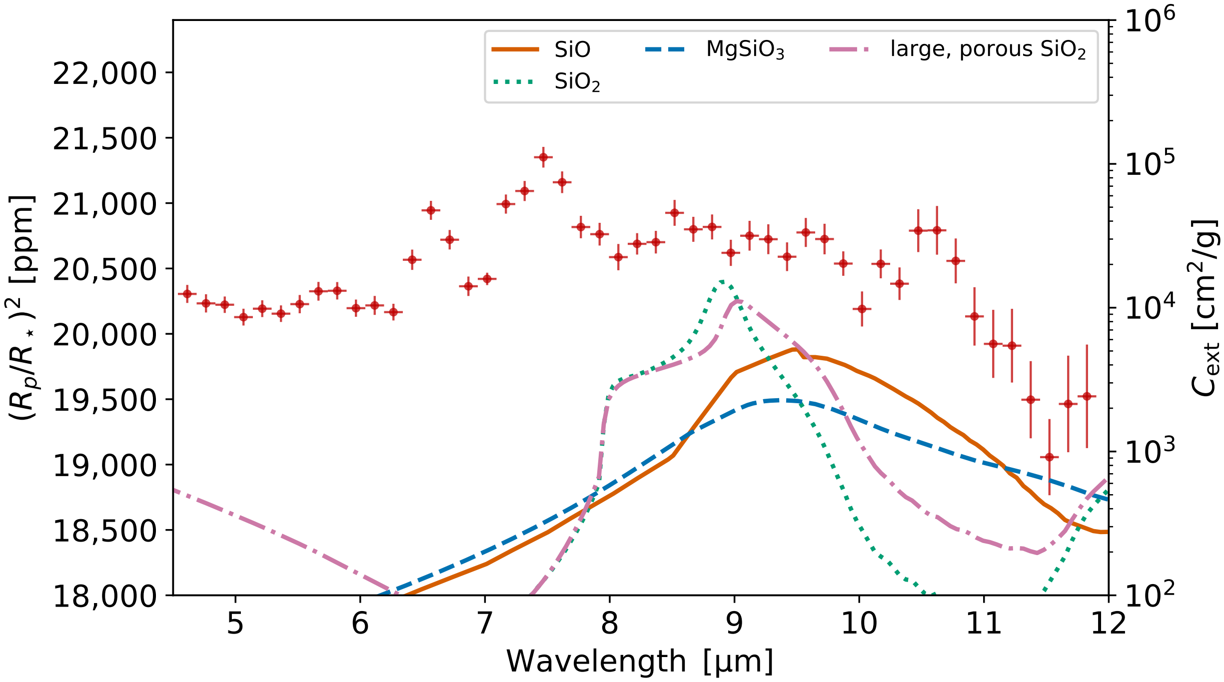


Suppl. Inf. – Figure 12: **Comparison of the extinction coefficient of the silicate cloud particles with the transit spectrum of WASP-107b.** The extinction curves are computed for $0.01$ $\mu$m solid particles for SiO (red), $SiO_2$ (green) and $MgSiO_3$ (blue), representative of the particle size found by the `ARCiS` retrievals. The pink curve is computed using a size distribution of particles between $0.1$ and $2$ $\mu$m and a porosity of 0.25 (representative of the particles found by the `pRT` retrievals).

temperature-pressure profile ($T$-$P$) has been computed using the analytical equation derived by ref. [32], assuming an infrared (IR) atmosphere opacity $\kappa_{\rm IR} = 0.01$, a ratio between optical and IR opacity $\gamma = 0.4$, an equilibrium temperature $T_{\rm eq} = 740$ K, and an intrinsic temperature, $T_{\rm int}$, in the range of 250 – 600 K. Vertical mixing in 1D chemical models is commonly parameterized by eddy diffusion. However, for exoplanets, the eddy diffusion coefficient $K_{\rm zz}$ is loosely defined [109]. For the 1D photochemical models used in this work, we assume a constant $K_{\rm zz}$, with values varying between $10^8 - 10^{11}$ cm$^2$ s$^{-1}$. We explore a range of C/O ratios, from solar (0.55) to sub-solar (0.1), the lower limit informed by planet formation models [112] that predict a C/O ratio for the planet above $\sim$0.15. Our base model used in Extended Data Figure 3 has an intrinsic temperature of 400 K, a solar C/O ratio, a metallicity of 10$\times$ solar, and a $\log_{10}(K_{\rm zz}$, cgs$) = 10$.

Our 1D chemical kinetics model treats thermochemical and photochemical reactions. The thermochemical network is based on the C–H–N–O–S network from VULCAN [9] for reduced atmospheres containing 89 neutral C-, H-, O-, N-, and S-bearing species and 1028 total thermochemical reactions (i.e., 514 forward-backward pairs) [114]. The photo-absorption cross sections are taken from the KIDA database [115] and complemented with additional sulphur photo-absorption cross sections (O. Venot, private communication). The full network cross sections were benchmarked against WASP-39b [10].

The chemical model predictions are sensitive to the flux impinging the outer atmosphere. To simulate the spectral energy distribution (SED) of the host star WASP-107, we take the stellar spectrum of HD 85512, which is of similar spectral type (K6 V) and for which a panchromatic SED was constructed in the MUSCLES survey [34]. Being both K6 dwarf stars, the bolometric luminosity of both SEDs is similar, but the chromospheric and coronal activity can differ between both stars. To assess that difference, we observed contemporaneously with the JWST observations, the Near-Ultraviolet (NUV) emission of the host star WASP-107 with *Neil Gehrels Swift*. We also reanalysed the X-ray emission observed with *XMM-Newton* in 2018. The measured flux densities incident on WASP-107b yields a NUV flux value that is $\sim$6.4 erg cm$^{-2}$ s$^{-1}$ Å$^{-1}$ and an X-ray flux value that is $\sim 1 \times 10^3$ erg cm$^{-2}$ s$^{-1}$; see Sect. 2.1 –2.2. The folding of the MUSCLES HD 85512 spectrum with the *Swift* filter transmission curve yields a value that is lower by only $\sim$30% compared to WASP-107, while the X-ray emission of HD 85512 is lower by a factor of $\sim$20. The rotation period of $\sim$47 days [118] implies an age of $\sim$5.6 Gyr for HD 85512, hence considerably older than WASP-107 with an estimated age of $\sim$3.4 Gyr [2]. Therefore, it is not unexpected that HD 85512 is significantly less magnetic and/or has less coronal activity than WASP-107. However, for our photochemical models mainly the NUV and FUV flux is of importance, since the X-ray emission primarily impacts photoionization which is not included in our models. We therefore can use the MUSCLES HD 85512 spectrum as representation of WASP-107's SED.

Each chemical model was executed with a vertical resolution comprising 130 layers spanning the pressure range from $10^{-7}$ to 100 bar. Subsequently, the hydrodynamical input and the abundances resulting from the chemical kinetics simulations are used to compute a synthetic transmission spectrum, using the radiative transfer package `petitRADTRANS` [14] (see above). Next to the line absorption opacities described in the `petitRADTRANS` retrieval setup, we also include the line absorption opacities listed in ref. [109]. Since the primary goal of the forward model computations is to understand the gas-phase formation of $SO_2$, $CH_4$ and $H_2O$ in this planet independent of cloud-formation, no condensate opacity was added in this last post-processing setup. For each pressure layer, the mean molecular weight is calculated based on the mixture that resulted from the disequilibrium chemistry models. The planetary radius at reference pressure (0.01 bar) was set to 0.9 $R_p$. Finally, the predicted synthetic spectra are rebinned to the spectral resolution of the WASP-107b JWST MIRI data.

### 4.2. (Photo)chemical model predictions

Figure 3 provides evidence that only models incorporating photochemistry in combination with a super-solar metallicity predict a detectable level of $SO_2$ in WASP-107b. The large atmospheric scale height of WASP-107b enables highly efficient photochemical processes to operate within the $\sim$740 K temperature regime of this low-density planet, resulting in $SO_2$ volume mixing ratios being $>5\times10^{-7}$ at pressures between $10^{-7} - 10^{-4}$ bar.

We explored the sensitivity of $SO_2$ to both the metallicity and the C/O ratio itself. Extended Data Figure 3 shows that the $SO_2$ molar fraction in the upper atmosphere of WASP-107b displays a mild sensitivity to the explored C/O ratio, increasing by a few factors as the C/O decreased from solar (0.55) to sub-solar (0.10). In contrast, the $SO_2$ molar fraction is highly sensitive to the metallicity (see Figure 3) owing to the fact that both the sulphur and oxygen abundance scale with metallicity. Our photochemical models show that $SO_2$ becomes detectable at super-solar metallicities, an effect already noted for higher temperature atmospheres [17].

Two critical parameters influencing the detectability of $SO_2$ within a planetary atmosphere are the UV irradiation and the gravity ($g$), which in turn determines the atmospheric scale height (see Extended Data Figure 1). Although the atmospheric scale height for both WASP-107b and WASP-39b is roughly equivalent (estimated at $\sim 1 \times 10^6$ m), their gravity differs, with WASP-107b at $\sim$260 cm/s$^2$ and WASP-39b at $\sim$430 cm/s$^2$. It is important to note that simulations of WASP-39b in previous studies were conducted at higher gravity values of 1,000 cm/s$^2$ [10] and 2,140 m/s$^2$ [17]. Extended Data Figure 1 juxtaposes the $SO_2$ predictions under $g = 260$ cm/s$^2$ and $g = 430$ cm/s$^2$ (similar to WASP-39b) and 1,000 cm/s$^2$, where the gravity has been adapted by scaling the mass of the planet. While the increase of gravity from 260 cm/s$^2$ to 430 cm/s$^2$ only slightly alters the $SO_2$ abundance profile, a gravity of 1,000 cm/s$^2$ significantly decreases the $SO_2$ abundance at pressures between $\sim 10^{-5} - 1$ bar. This is attributed to the reduced efficiency of photochemistry in deeper layers of atmospheres with high gravity. Consequently, this reduction diminishes the reservoir of OH radicals necessary for the synthesis of $SO_2$.

A last simulation employs a gravitational force of 260 cm/s$^2$ as well, but uses the SED of HD 85512 - as a proxy for WASP-107 - scaled by a factor 100 (brown line in Extended Data Figure 1) or the WASP-39 spectrum from Ref. [10] (purple line in Extended Data Figure 1) as the input stellar spectrum. The flux density originating from the host star, incident at the planet, is approximately 200 times greater for WASP-39b than for WASP-107b in the near-ultraviolet (NUV) range, and exhibits a factor of $\sim$100 – 1,000 in the far-ultraviolet (FUV), with comparable EUV and X-ray fluxes (see Suppl. Inf. Figure 13). Photodissociation of $SO_2$ and $H_2S$ mainly operates in the FUV, with absorption cross sections reaching around $10^{-16}$ cm$^2$. While the NUV absorption cross sections for $SO_2$ are about two orders of magnitude lower than in the FUV, it's worth noting that the $H_2S$ cross sections are only available up to $\sim$250 nm; see Suppl. Inf. Figure 13.

Increasing the UV irradiation with a factor 100 triggers the direct photodissociation of $SO_2$ at altitudes near $10^{-4}$ bar. At higher altitudes, this process is somewhat counteracted by $H_2O$ photolysis, generating additional OH radicals that react with S and SO to form $SO_2$ (see brown line in Extended Data Figure 1). However, when adopting the WASP-39 spectrum with its more extreme FUV/NUV ratio, an interesting observation emerges (purple line in Extended Data Figure 1): around $10^{-3}$ bar, direct FUV-driven photodissociation of $SO_2$ takes place, while at altitudes near $10^{-4}$ bar, the additional destruction of $H_2S$ liberates sulphur radicals. These sulphur atoms are subsequently oxidized into $SO_2$, partially offsetting the $SO_2$ loss at deeper levels. At the uppermost atmospheric levels, approximately several times $10^{-7}$ bar, $SO_2$ undergoes photodissociation across all simulations. Hence, a low gravity together with modest UV irradiation and FUV/NUV ratio are

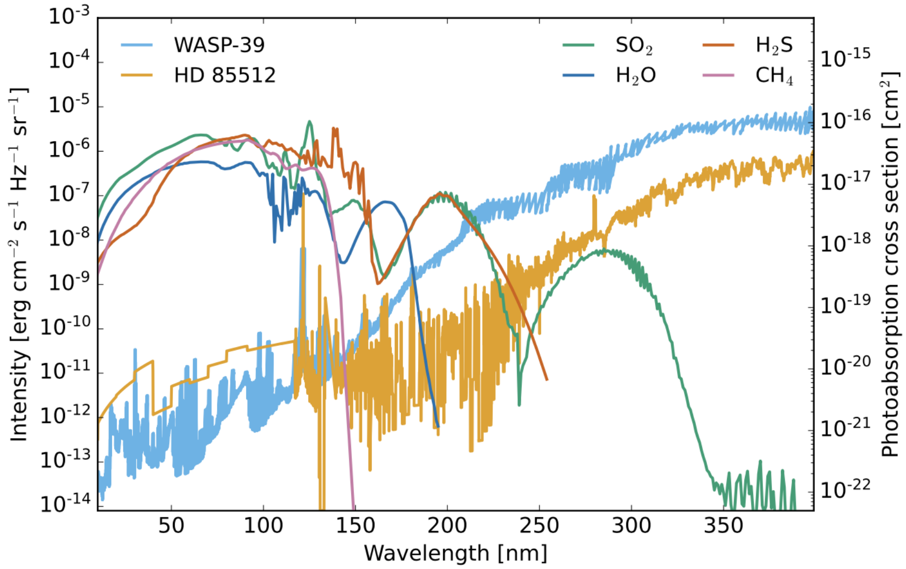


Suppl. Inf. – Figure 13: **Input stellar spectral energy distributions (SED) and photo-absorption cross sections.** The orange and light blue curve show the SED of HD 85512 – used as proxy for WASP-107 – and of WASP-39, with corresponding intensity values given on the left y-axis. The photo-absorption cross sections of $SO_2$, $H_2O$, $H_2S$, and $CH_4$ are shown in green, pink, dark blue, and brown, respectively, with corresponding values given on the right y-axis.

the key ingredients for the formation of $SO_2$ in detectable amounts.

Extended Data Figure 3 shows that the eddy diffusion and the intrinsic temperature have a minor impact on the abundance of $SO_2$ at those pressure levels where the MIRI $SO_2$ features predominantly emerge, i.e. at pressures below a few times $10^{-5}$ bar (see Extended Data Figure 4). Even when excluding vertical transport in the disequilibrium models ($K_{zz} = 0\,\mathrm{cm}^2\,\mathrm{s}^{-1}$) a significant abundance of $SO_2$ is still predicted at pressures below a few times $10^{-4}$ bar (see panel (b) in Suppl. Inf. Figure 14), proving the crucial role of photolysis in establishing the chemical composition in WASP-107b's atmosphere. The increase in $SO_2$ formation around $10^{-3}$ bar (for $K_{zz} = 0\,\mathrm{cm}^2\,\mathrm{s}^{-1}$, purple line) is caused by the breaking up of $H_2S$ yielding sulphur radicals that are subsequently oxidised. When including eddy diffusion, these sulphur atoms are redistributed through the atmosphere, resulting in a $SO_2$ molar fraction depicted with the full black line.

A chemical network analysis indicated that the primary trigger for the formation of $SO_2$ in the atmosphere of WASP-39b is water photolysis [10]. However, at first sight, it seems that water photolysis only plays a minor role for the production of $SO_2$ in WASP-107b. This conclusion is drawn from panel (b) in Suppl. Inf. Figure 14 where we exclude water photodissociation from our photochemical models (green line). It can be seen that the influence on the predicted $SO_2$ abundance is only confined to pressures below $10^{-5}$ bar. The reason for this behaviour is that $H_2O$ is predominantly photodissociated in the uppermost atmospheric layers. This is also shown in

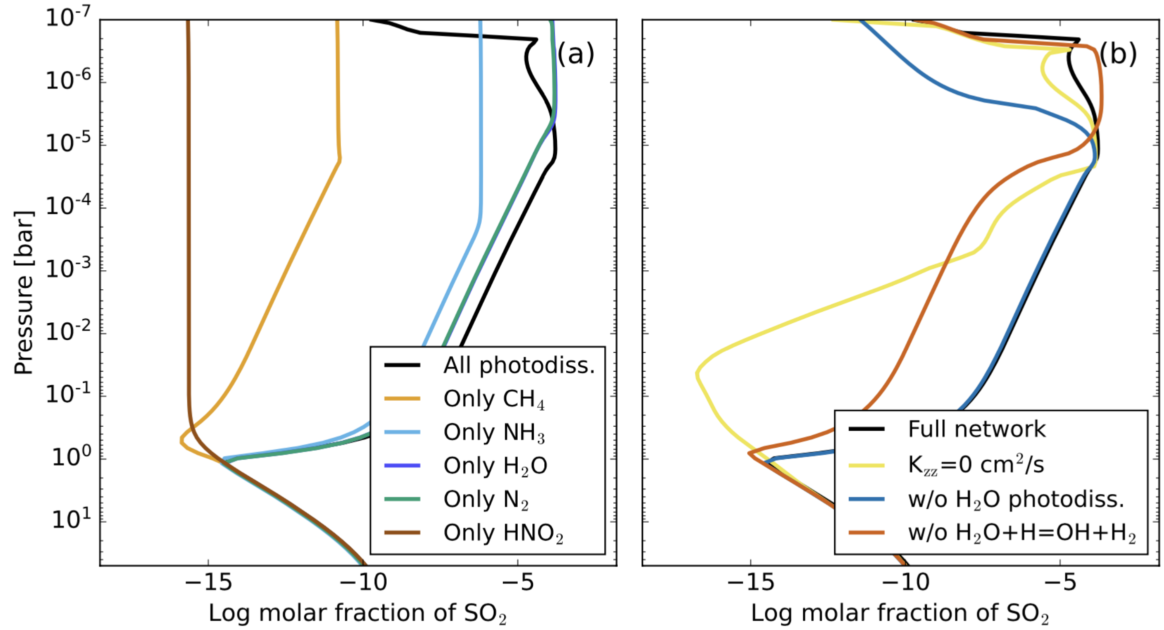


Suppl. Inf. – Figure 14: **$SO_2$ molar fraction predictions for WASP-107b for different set-ups of the photochemical network.** The base model (shown in black in each panel) has an intrinsic temperature of 400 K, a solar C/O ratio, a metallicity of 10× solar, a $\log_{10}(K_{zz}, \text{cgs}) = 10$, and uses the SED of HD 85512 - used as a proxy for WASP-107 - as input stellar spectrum. Panel (a): Predicted $SO_2$ molar fractions when all photo-absorption cross sections (black) are taken into account during the chemistry simulation, compared to predictions where only $CH_4$ (orange), $NH_3$ (light blue), $H_2O$ (dark blue), $N_2$ (green) or $HNO_2$ (brown) are used. Panel (b): Predicted $SO_2$ molar fractions without vertical mixing, i.e. $K_{zz} = 0\,\text{cm}^2/\text{s}$ (yellow), without photodissociation of $H_2O$ (blue), and without including the thermochemical reaction $H_2O+H \rightleftharpoons H_2+OH$ (orange).

panel (b) of Suppl. Inf. Figure 15 where we compare the [OH]/[H] ratio under equilibrium and disequilibrium conditions. While the omission of $H_2O$ photodissociation explains the difference between both curves for pressures around a few times $10^{-7}$ bar, the vertical transport is the main reason for the difference between equilibrium and disequilibrium predictions for pressures between $\sim 10^{-4} - 1$ bar. The thermochemical reaction of main importance for establishing the [OH]/[H] ratio in that pressure regime (see panel (b) in Suppl. Inf. Figure 14) is

$$H_2O+H \underset{k_r}{\overset{k_f}{\rightleftharpoons}} H_2 + OH. \tag{4}$$

The reverse reaction rate, $k_r$, is given in the VULCAN network in its Arrhenius form

$$k_r = A_r\, T_r^B\, \exp(-C_r/T)\ \ [\text{cm}^3\ \text{s}^{-1}]\,, \tag{5}$$

with $T$ the temperature (in Kelvin), and the corresponding parameters being the pre-exponential factor $A_r = 3.57 \times 10^{-16}\,\text{cm}^3\ \text{s}^{-1}$, the temperature-dependent exponent $B_r = 1.52$, and the activation energy $C_r = 1740$ K. Using the NTRS-NASA thermodynamic data [120] and assuming thermodynamic equilibrium, the Gibbs free energy of formation of the forward reaction, and the corresponding equilibrium constant can be calculated [121]. This allows the calculation of the forward reaction rate $k_f$. Fitting these results with the Arrhenius form yields $A_f = 1.54 \times 10^{-14}$ cm$^3$ s$^{-1}$, $B_f = 1.245$, and a high energy barrier of $C_f = 9468$ K. It can be seen that at the temperatures relevant for planet atmospheres, the forward reaction rate is much lower than the reverse rate.

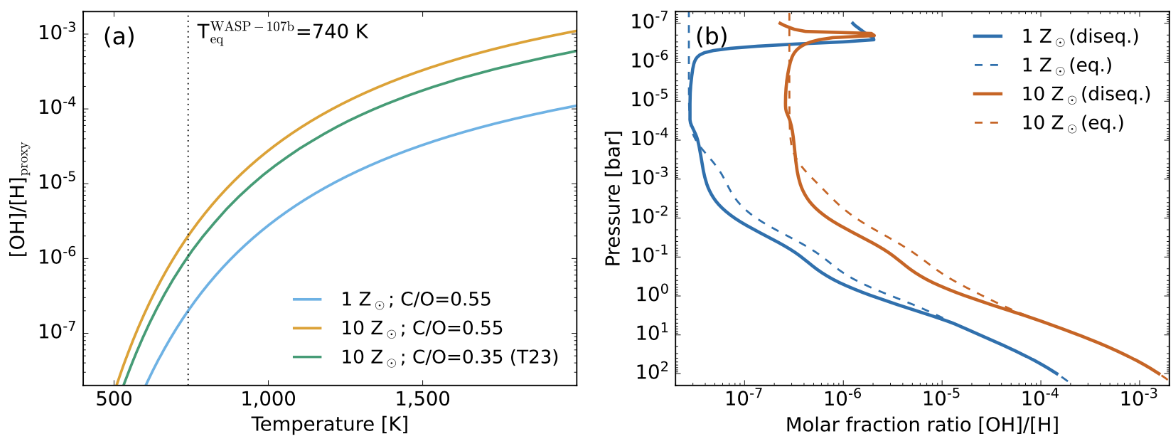


Suppl. Inf. – Figure 15: **[OH]/[H] ratio for equilibrium and disequilibrium predictions.** Panel (a): Proxy for the [OH]/[H] ratio assuming thermodynamic equilibrium and that most of the O is in $H_2O$ at solar metallicity (blue) and at $Z = 10\,Z_\odot$ (orange). The prediction by Ref. [10] is shown as a green line for comparison. Panel (b): The molar fraction of [OH]/[H] under two conditions: solar metallicity (blue) and 10× solar metallicity (orange), is depicted in both chemical equilibrium (dashed line) and disequilibrium (solid line) calculations.

Similar to Ref. [10], we then can calculate the [OH]/[H] ratio assuming thermodynamic equilibrium and that most of the O is in $H_2O$. This yields panel (a) in Suppl. Inf. Figure 15, to be compared with Extended Data Figure 10 of Ref. [10]. At temperatures below $\sim$750 K, the [OH]/[H] ratio drops below $\sim 2 \times 10^{-6}$ for $Z = 10\,Z_\odot$, and hence a factor 10 lower at solar metallicity. This scarcity of OH has been used as an argument for the lack of $SO_2$ formation at equilibrium temperatures below approximately $\sim$1,000 K for a planet with WASP-39b parameters, favouring instead the prevalence of sulphur allotropes $S_x$ [10].

The central inquiry that emerges is how $SO_2$ can be created within the atmosphere of WASP-107b if the aforementioned argument stands. The solution becomes evident through Suppl. Inf. Figure 14, where it is demonstrated that the photodissociation of various specific abundant molecules sparks the generation of $SO_2$. This assertion is exemplified in panel (a) of Suppl. Inf. Figure 14, where the photodissociation of either only $H_2O$ (or only $N_2$ or $NH_3$) leads to the emergence of $SO_2$. But the photodissociation of only $CH_4$ (only acting at wavelengths $\lesssim$140 nm; see Suppl. Inf. Figure 13) yields negligible amounts of $SO_2$, while the photodissociation of the rare molecule $HNO_2$

yields outcomes consistent with chemical equilibrium predictions, wherein all photodissociation is thus excluded (see dotted line in panel (b) of Figure 3). This phenomenon arises from the fact that the photodissociation of various specific abundant molecules releases atoms and radicals that induce a very active photochemistry even down to pressure layers of approximately 1 bar. Reactions involving the liberated atoms and radicals often display temperature-independent behaviour without energy barriers (i.e., $B = C = 0$) and possess pre-exponential factors typically on the order of $10^{-11} - 10^{-7}\,\mathrm{cm^3\,s^{-1}}$. Consequently, a significant amount of H atoms and OH radicals is formed, leading to the oxidisation of sulphur into $SO_2$. Hence, although the photolysis of $H_2O$ can initiate the production of $SO_2$ in WASP-107b, it is not the sole molecule whose photodissociation holds the potential to induce $SO_2$ formation.

In summary, the overarching scenario that unfolds reveals that the primary pathways initiating the formation of $SO_2$ in the low-density atmosphere of WASP-107b are twofold. Firstly, through the photodissociation of $H_2O$ in the upper atmospheric layers at pressures below a few times $10^{-6}$ bar, yielding atomic H and OH radicals. These OH radicals are key for oxidising sulphur that is liberated from $H_2S$. Secondly, in the pressure range of $10^{-5} - 1$ bar, the prevailing determinant of the chemical composition is the interplay of photochemical processes acting upon various abundant molecules, not limited to $H_2O$. These processes can generate a sufficiently substantial quantity of free atoms and radicals, that can be redistributed through eddy diffusion. This initiates a cascade of barrierless thermochemical reactions that progressively culminate in the formation of $SO_2$. Given the fact that a large ensemble of those reactions are temperature-independent, the equilibrium temperature stands as just one among several factors dictating the formation (or not) of $SO_2$. As long as the UV irradiation and FUV/NUV ratio remain moderate and the gravity is low, these processes will lead to the formation of $SO_2$ in sufficient amounts to be detectable even within a $\sim$740 K temperature planet.

# Supplementary References


35. Kendrew, S. *et al.* The Mid-Infrared Instrument for the James Webb Space Telescope, IV: The Low-Resolution Spectrometer. *Pub. Astron. Soc. Pacific* **127**, 623 (2015).

36. Rieke, G. H. *et al.* The Mid-Infrared Instrument for the James Webb Space Telescope, I: Introduction. *Pub. Astron. Soc. Pacific* **127**, 584 (2015).

37. Ressler, M. E. *et al.* The Mid-Infrared Instrument for the James Webb Space Telescope, VIII: The MIRI Focal Plane System. *Pub. Astron. Soc. Pacific* **127**, 675 (2015).

38. Bouwman, J. *et al.* Spectroscopic Time Series Performance of the Mid-infrared Instrument on the JWST. *Pub. Astron. Soc. Pacific* **135**, 038002 (2023).

39. Bell, T. *et al.* Eureka!: An End-to-End Pipeline for JWST Time-Series Observations. *The Journal of Open Source Software* **7**, 4503 (2022).

40. Bell, T. J. *et al.* A First Look at the JWST MIRI/LRS Phase Curve of WASP-43b (2023).

41. Anderson, D. R., Collier Cameron, A. & Delrez, L. The discoveries of WASP-91b, WASP-105b and WASP-107b: Two warm Jupiters and a planet in the transition region between ice giants and gas giants. *Astron. Astrophys.* **604**, A110 (2017).

42. Ivshina, E. S. & Winn, J. N. TESS Transit Timing of Hundreds of Hot Jupiters. *Astrophys. J. Suppl.* **259**, 62 (2022).

43. Dai, F. & Winn, J. N. The Oblique Orbit of WASP-107b from K2 Photometry. *Astron. J.* **153**, 205 (2017).

44. Morello, G. *et al.* The ExoTETHyS Package: Tools for Exoplanetary Transits around Host Stars. *Astron. J.* **159**, 75 (2020).

45. Kipping, D. M. Efficient, uninformative sampling of limb darkening coefficients for two-parameter laws. *Mon. Not. Roy. Astron. Soc.* **435**, 2152–2160 (2013).

46. Piaulet, C. *et al.* WASP-107b's Density Is Even Lower: A Case Study for the Physics of Planetary Gas Envelope Accretion and Orbital Migration. *Astron. J.* **161**, 70 (2021).

47. Morrison, J. JWST MIRI flight performance: Detector Effects and Data Reduction Algorithms. *in prep.* (2023).

48. Carone, L. *et al.* Indications for very high metallicity and absence of methane in the eccentric exo-Saturn WASP-117b. *Astron. Astrophys.* **646**, A168 (2021).

49. Argyriou, I. Calibration of the MIRI instrument on board the James Webb Space Telescope (2021).

50. Foreman-Mackey, D., Hogg, D. W., Lang, D. & Goodman, J. emcee: The MCMC Hammer. *Pub. Astron. Soc. Pacific* **125**, 306 (2013).

51. Kreidberg, L. batman: BAsic Transit Model cAlculatioN in Python. *Pub. Astron. Soc. Pacific* **127**, 1161 (2015).

52. Kumar, R., Carroll, C., Hartikainen, A. & Martin, O. A. ArviZ a unified library for exploratory analysis of Bayesian models in Python. *The Journal of Open Source Software* (2019).

53. Foreman-Mackey, D. *et al.* exoplanet: Gradient-based probabilistic inference for exoplanet data & other astronomical time series. *The Journal of Open Source Software* **6**, 3285 (2021).

54. Argyriou, I. *et al.* The Brighter-Fatter Effect in the JWST MIRI Si:As IBC detectors I. Observations, impact on science, and modelling. *arXiv e-prints* arXiv:2303.13517 (2023).

55. Pontoppidan, K. M. *et al.* Pandeia: a multi-mission exposure time calculator for JWST and WFIRST. In Peck, A. B., Benn, C. R. & Seaman, R. L. (eds.) *Observatory Operations: Strategies, Processes, and Systems VI*, 44 (SPIE, Edinburgh, United Kingdom, 2016).

56. Carone, L. *et al.* Equatorial retrograde flow in WASP-43b elicited by deep wind jets? *Mon. Not. Roy. Astron. Soc.* **496**, 3582–3614 (2020).

57. Roming, P. W. A. *et al.* The Swift Ultra-Violet/Optical Telescope. *Space Science Rev.* **120**, 95–142 (2005).

58. Salz, M. *et al.* Swift UVOT near-UV transit observations of WASP-121 b. *Astron. Astrophys.* **623**, A57 (2019).

59. Poole, T. S. *et al.* Photometric calibration of the Swift ultraviolet/optical telescope: Photometric calibration of the Swift UVOT. *Mon. Not. Roy. Astron. Soc.* **383**, 627–645 (2007).

60. Bertin, E. & Arnouts, S. SExtractor: Software for source extraction. *Astron. Astrophys. Suppl.* **117**, 393–404 (1996).

61. Taylor, M. B. TOPCAT & STIL: Starlink Table/VOTable Processing Software. In Shopbell, P., Britton, M. & Ebert, R. (eds.) *Astronomical Data Analysis Software and Systems XIV*, vol. 347 of *Astron. Soc. Pacific Conf. Series*, 29 (2005).

62. Breeveld, A. A. *et al.* An Updated Ultraviolet Calibration for the Swift/UVOT. In McEnery, J. E., Racusin, J. L. & Gehrels, N. (eds.) *Gamma Ray Bursts 2010*, vol. 1358 of *American Institute of Physics Conference Series*, 373–376 (2011).

63. Woods, T. N. *et al.* Solar Irradiance Reference Spectra (SIRS) for the 2008 Whole Heliosphere Interval (WHI). *Geophys. Res. Lett.* **36**, L01101 (2009).

64. Strüder, L. *et al.* The European Photon Imaging Camera on XMM-Newton: The pn-CCD camera. *Astron. Astrophys.* **365**, L18–L26 (2001).

65. Turner, M. J. L. *et al.* The European Photon Imaging Camera on XMM-Newton: The MOS cameras. *Astron. Astrophys.* **365**, L27–L35 (2001).

66. Webb, N. A. *et al.* The *XMM-Newton* serendipitous survey: IX. The fourth *XMM-Newton* serendipitous source catalogue. *Astron. Astrophys.* **641**, A136 (2020).

67. Nortmann, L. *et al.* Ground-based detection of an extended helium atmosphere in the Saturn-mass exoplanet WASP-69b. *Science* **362**, 1388–1391 (2018).

68. Foster, G., Poppenhaeger, K., Ilic, N. & Schwope, A. Exoplanet X-ray irradiation and evaporation rates with eROSITA. *Astron. Astrophys.* **661**, A23 (2022).

69. Spinelli, R. *et al.* Planetary Parameters, XUV Environments, and Mass-loss Rates for Nearby Gaseous Planets with X-Ray-detected Host Stars. *Astron. J.* **165**, 200 (2023).

70. Arnaud, K. A. XSPEC: The First Ten Years. In Jacoby, G. H. & Barnes, J. (eds.) *Astronomical Data Analysis Software and Systems V*, vol. 101 of *Astron. Soc. Pacific Conf. Series*, 17 (1996).

71. Johnstone, C. P. & Güdel, M. The coronal temperatures of low-mass main-sequence stars. *Astron. Astrophys.* **578**, A129 (2015).

72. Močnik, T., Hellier, C., Anderson, D. R., Clark, B. J. M. & Southworth, J. Starspots on WASP-107 and pulsations of WASP-118. *Mon. Not. Roy. Astron. Soc.* **469**, 1622–1629 (2017).

73. Johnstone, C. P., Bartel, M. & Güdel, M. The active lives of stars: A complete description of the rotation and XUV evolution of F, G, K, and M dwarfs. *Astron. Astrophys.* **649**, A96 (2021).

74. Kreidberg, L., Line, M. R., Thorngren, D., Morley, C. V. & Stevenson, K. B. Water, High-altitude Condensates, and Possible Methane Depletion in the Atmosphere of the Warm Super-Neptune WASP-107b. *Astrophys. J. Lett.* **858**, L6 (2018).

75. Min, M., Ormel, C. W., Chubb, K., Helling, C. & Kawashima, Y. The ARCiS framework for exoplanet atmospheres. Modelling philosophy and retrieval. *Astron. Astrophys.* **642**, A28 (2020).

76. Mollière, P. *et al.* petitRADTRANS. A Python radiative transfer package for exoplanet characterization and retrieval. *Astron. Astrophys.* **627**, A67 (2019).

77. Polyansky, O. L. *et al.* ExoMol molecular line lists XXX: a complete high-accuracy line list for water. *Mon. Not. Roy. Astron. Soc.* **480**, 2597–2608 (2018).

78. Rothman, L. S. *et al.* HITEMP, the high-temperature molecular spectroscopic database. *J. Quant. Spectrosc. Radiat. Transfer* **111**, 2139–2150 (2010).

79. Yurchenko, S. N., Mellor, T. M., Freedman, R. S. & Tennyson, J. ExoMol line lists – XXXIX. Ro-vibrational molecular line list for CO2. *Mon. Not. Roy. Astron. Soc.* **496**, 5282–5291 (2020).

80. Yurchenko, S. N., Amundsen, D. S., Tennyson, J. & Waldmann, I. P. A hybrid line list for $CH_4$ and hot methane continuum. *Astron. Astrophys.* **605**, A95 (2017).

81. Chubb, K. L., Tennyson, J. & Yurchenko, S. N. ExoMol molecular line lists - XXXVII. Spectra of acetylene. *Mon. Not. Roy. Astron. Soc.* **493**, 1531–1545 (2020).

82. Underwood, D. S. *et al.* ExoMol molecular line lists – XIV. The rotation–vibration spectrum of hot SO2. *Mon. Not. Roy. Astron. Soc.* **459**, 3890–3899 (2016).

83. Bernath, P. F., Johnson, R. M. & Liévin, J. Line lists for $X^3\Sigma^-$ and $a^1\Delta$ vibration-rotation bands of SO. *J. Quant. Spectrosc. Radiat. Transfer* **290**, 108317 (2022).

84. Azzam, A. A. A., Tennyson, J., Yurchenko, S. N. & Naumenko, O. V. ExoMol molecular line lists – XVI. The rotation–vibration spectrum of hot H2S. *Mon. Not. Roy. Astron. Soc.* **460**, 4063–4074 (2016).

85. Barton, E. J., Yurchenko, S. N. & Tennyson, J. ExoMol line lists – II. The ro-vibrational spectrum of SiO. *Mon. Not. Roy. Astron. Soc.* **434**, 1469–1475 (2013).

86. Barber, R. J. *et al.* ExoMol line lists – III. An improved hot rotation-vibration line list for HCN and HNC. *Mon. Not. Roy. Astron. Soc.* **437**, 1828–1835 (2013).

87. Coles, P. A., Yurchenko, S. N. & Tennyson, J. ExoMol molecular line lists – XXXV. A rotation-vibration line list for hot ammonia. *Mon. Not. Roy. Astron. Soc.* **490**, 4638–4647 (2019).

88. Sousa-Silva, C., Al-Refaie, A. F., Tennyson, J. & Yurchenko, S. N. ExoMol line lists – VII. The rotation–vibration spectrum of phosphine up to 1500 K. *Mon. Not. Roy. Astron. Soc.* **446**, 2337–2347 (2014).

89. Chubb, K. L. *et al.* The ExoMolOP database: Cross sections and k-tables for molecules of interest in high-temperature exoplanet atmospheres. *Astron. Astrophys.* **646**, A21 (2021).

90. Jäger, C., Dorschner, J., Mutschke, H., Posch, T. & Henning, T. Steps toward interstellar silicate mineralogy. VII. Spectral properties and crystallization behaviour of magnesium silicates produced by the sol-gel method. *Astron. Astrophys.* **408**, 193–204 (2003).

91. Henning, T. & Mutschke, H. Low-temperature infrared properties of cosmic dust analogues. *Astron. Astrophys.* **327**, 743–754 (1997).

92. Palik, E. *Handbook of Optical Constants of Solids*. Bd. 1 (Elsevier Science, 2012).

93. Kitzmann, D. & Heng, K. Optical properties of potential condensates in exoplanetary atmospheres. *Mon. Not. Roy. Astron. Soc.* **475**, 94–107 (2018).

94. Wetzel, S., Klevenz, M., Gail, H. P., Pucci, A. & Trieloff, M. Laboratory measurement of optical constants of solid SiO and application to circumstellar dust. *Astron. Astrophys.* **553**, A92 (2013).

95. Zubko, V. G., Mennella, V., Colangeli, L. & Bussoletti, E. Optical constants of cosmic carbon analogue grains - I. Simulation of clustering by a modified continuous distribution of ellipsoids. *Mon. Not. Roy. Astron. Soc.* **282**, 1321–1329 (1996).

96. Min, M., Hovenier, J. W. & de Koter, A. Modeling optical properties of cosmic dust grains using a distribution of hollow spheres. *Astron. Astrophys.* **432**, 909–920 (2005).

97. Benneke, B. & Seager, S. How to Distinguish between Cloudy Mini-Neptunes and Water/Volatile-Dominated Super-Earths. *Astrophys. J.* **778**, 153 (2013).

98. Dalgarno, A. & Williams, D. A. Rayleigh Scattering by Molecular Hydrogen. *Astrophys. J.* **136**, 690–692 (1962).

99. Chan, Y. M. & Dalgarno, A. The refractive index of helium. *Proceedings of the Physical Society* **85**, 227 (1965).

100. Borysow, J., Frommhold, L. & Birnbaum, G. Collison-induced rototranslational absorption spectra of $H_2$-He pairs at temperatures from 40 to 3000 K. *Astrophys. J.* **326**, 509–515 (1988).

101. Borysow, A., Frommhold, L. & Moraldi, M. Collision-induced infrared spectra of $H_2$-He pairs involving 0-1 vibrational transitions and temperatures from 18 to 7000 K. *Astrophys. J.* **336**, 495–503 (1989).

102. Borysow, A. & Frommhold, L. Collision-induced infrared spectra of $H_2$-He pairs at temperatures from 18 to 7000 K. II - Overtone and hot bands. *Astrophys. J.* **341**, 549–555 (1989).

103. Borysow, A., Jorgensen, U. G. & Fu, Y. High-temperature (1000-7000 K) collision-induced absorption of $H_2$ pairs computed from the first principles, with application to cool and dense stellar atmospheres. *J. Quant. Spectrosc. Radiat. Transfer* **68**, 235–255 (2001).

104. Borysow, A. Collision-induced absorption coefficients of $H_2$ pairs at temperatures from 60 K to 1000 K. *Astron. Astrophys.* **390**, 779–782 (2002).

105. Richard, C. *et al.* New section of the HITRAN database: Collision-induced absorption (CIA). *J. Quant. Spectrosc. Radiat. Transfer* **113**, 1276–1285 (2012).

106. Scott, A. & Duley, W. W. Ultraviolet and Infrared Refractive Indices of Amorphous Silicates. *Astrophys. J. Suppl.* **105**, 401 (1996).

107. Ackerman, A. S. & Marley, M. S. Precipitating Condensation Clouds in Substellar Atmospheres. *Astrophys. J.* **556**, 872–884 (2001).

108. Hejazi, N. *et al.* Elemental Abundances of the Super-Neptune WASP-107b's Host Star Using High-resolution, Near-infrared Spectroscopy. *The Astrophysical Journal* **949**, 79 (2023).

109. Baeyens, R. *et al.* Grid of pseudo-2D chemistry models for tidally locked exoplanets - I. The role of vertical and horizontal mixing. *Mon. Not. Roy. Astron. Soc.* **505**, 5603–5653 (2021).

110. Agúndez, M., Venot, O., Selsis, F. & Iro, N. The Puzzling Chemical Composition of GJ 436b's Atmosphere: Influence of Tidal Heating on the Chemistry. *Astrophys. J.* **781**, 68 (2014).

111. Guillot, T. On the radiative equilibrium of irradiated planetary atmospheres. *Astron. Astrophys.* **520**, A27 (2010).

112. Khorshid, N., Min, M., Désert, J. M., Woitke, P. & Dominik, C. SimAb: A simple, fast, and flexible model to assess the effects of planet formation on the atmospheric composition of gas giants. *Astron. Astrophys.* **667**, A147 (2022).

113. Tsai, S.-M., Malik, M. & Kitzmann, D. A Comparative Study of Atmospheric Chemistry with VULCAN. *Astrophys. J.* **923**, 264 (2021).

114. Baeyens, R., Désert, J.-M., Petrignani, A., Carone, L. & Schneider, A. D. Photodissociation and induced chemical asymmetries on ultra-hot gas giants. A case study of HCN on WASP-76 b. *arXiv e-prints* arXiv:2309.00573 (2023).

115. Venot, O. *et al.* New chemical scheme for giant planet thermochemistry. Update of the methanol chemistry and new reduced chemical scheme. *Astron. Astrophys.* **634**, A78 (2020).

116. Tsai, S.-M. *et al.* Photochemically produced $SO_2$ in the atmosphere of WASP-39b. *Nature* **617**, 483–487 (2023).

117. Loyd, R. O. P. *et al.* The MUSCLES Treasury Survey. III. X-Ray to Infrared Spectra of 11 M and K Stars Hosting Planets. *Astrophys. J.* **824**, 102 (2016).

118. France, K. *et al.* The MUSCLES Treasury Survey. I. Motivation and Overview. *Astrophys. J.* **820**, 89 (2016).

119. Polman, J., Waters, L. B. F. M., Min, M., Miguel, Y. & Khorshid, N. $H_2S$ and $SO_2$ detectability in hot Jupiters. Sulphur species as indicators of metallicity and C/O ratio. *Astron. Astrophys.* **670**, A161 (2023).

120. McBride, B. J., Gordon, S. & Reno, M. A. Thermodynamic data for fifty reference elements (2001).

121. Gail, H.-P. & Sedlmayr, E. *Physics and Chemistry of Circumstellar Dust Shells* (2013).